ENHANCED DROOP CONTROL WITH INTEGRATED SYNCHRONOUS MACHINE EMULATOR CHARACTERISTICS FOR GRID FORMING INVERTERS.

by

Kushal Buch

A thesis submitted to the faculty of
The University of North Carolina at Charlotte
in partial fulfillment of the requirements
for the degree of Master of Science in
Electrical Engineering

Charlotte

2024

Approved by:

____

Dr. Madhav Manjrekar

____

Dr. Babak Parkhideh

____

Dr. Valentina Cecchi

ABSTRACT

KUSHAL BUCH. Enhanced Droop Control with Integrated Synchronous Machine Emulator Characteristics for Grid Forming Inverters.. (Under the direction of DR. MADHAV MANJREKAR)

As power generation shifts towards cleaner energy, there is a growing effort to reduce the reliance on traditional fossil fuel-operated synchronous generators by adopting modern inverter-based resources. This rapid integration of inverter-based resources with the power grid has necessitated the development of advanced inverter controls. Existing controls of power electronic converter-based resources may not be sufficient to ensure grid stability in a future inverter-dominated power system. The grid-forming inverters have been considered as a potential solution to this emerging problem. Droop control is a widely used methodology in grid-forming inverters, especially due to its capabilities to enable power-sharing, frequency control, and voltage control. Recent advancements in droop control have incorporated filtering techniques (especially low pass filters) to mitigate AC harmonic noise injected into the control loops, thereby enhancing the overall response of the system. This research introduces the mathematical significance of the low pass filter used with droop control and establishes its necessity to enable grid-forming characteristics. Furthermore, an enhanced droop control is proposed with an integrated synchronous machine emulator using an error correction term. This enhanced droop control retains the benefits of conventional droop control but with the additive benefits of emulating the synchronous generator's response. These mathematical justifications are verified using bode plots, step responses, and eigenvalue analysis. The performance of the proposed controller and the grid-forming characteristics are verified using MATLAB simulations. These simulation results and the proposed controller's performance are verified by a controller hardware-in-loop experiment.

DEDICATION

I dedicate this research thesis to the guiding lights of my life, whose unwavering support and encouragement have been the cornerstone of my academic journey.

To my beloved parents, Rashesh Buch and Meena Buch, your boundless love, sacrifices, and tireless efforts have sculpted the person I am today. This achievement bears the indelible mark of your unwavering belief in me, and I am profoundly grateful for the deep impact of your guidance and encouragement.

To my dear brother, Jyot Buch, your steadfast support, understanding, and unwavering camaraderie have been the bedrock of strength throughout this academic journey. Your presence has illuminated even the darkest paths, transforming challenges into opportunities and successes into cherished moments of celebration.

This thesis stands as a tribute to the profound influence of these remarkable individuals in shaping my academic journey. Thank you for being the guiding stars that have illuminated my path to success.

ACKNOWLEDGEMENTS

I express my sincere gratitude to the individuals and entities whose unwavering support and guidance have been instrumental in the completion of this research journey.

My heartfelt thanks to my academic advisor, **Dr. Madhav Manjrekar**, for your expertise, mentorship, and insightful guidance throughout the research process. Your commitment to fostering intellectual growth has been a driving force behind the development of this work.

I extend my appreciation to the committee members, Dr. Babak Parkhideh and Dr. Valentina Cecchi, for their valuable contributions, feedback, and expertise. Your insights have added depth and rigor to this research.

To Prithwiraj, a dedicated supporter of college and research, your encouragement and belief in the significance of academic exploration have been invaluable.

Lastly, my gratitude to the entire Energy Production & Infrastructure Center (EPIC) for providing a stimulating academic environment. The collective efforts of the EPIC community have created a platform for meaningful research and academic growth.

This work stands as a testament to the collaborative spirit and support of these exceptional individuals and entities. Thank you for being integral parts of this academic journey.

TABLE OF CONTENTS

LIST OF TABLES

LIST OF FIGURES

LIST OF ABBREVIATIONS

AC: Alternating Current.

ADC: Analog to Digital Converter

AGC: Automatic Generation Control

AQC: Automatic Reactive Power Control

AVR: Automatic Voltage Regulator

CHIL: Controller Hardware-In-Loop

EMF: Electromotive Force.

EnDC-InSME: Enhanced Droop Control with Integrated Synchronous Machine Emulation

GFL: Grid Following Inverters.

GFM: Grid Forming Inverters.

HIL: Hardware-In-Loop

IBRs: Inverter Based Resources.

LPF: Low Pass Filter

PLL: Phase Lock Loop

SG: Synchronous Generator

SME-EDC: Synchronous Machine Emulator with Embedded Droop Control

TI: Texas Instruments

VSG: Virtual Synchronous Generator

CHAPTER 1: INTRODUCTION

The stability of the electric grid is implanted in decades of experience with the inertial properties and control framework of large synchronous generators (SG) ranging from hundreds to thousands of megawatts. Today's electric grid is rapidly transitioning towards clean energy specifically non-traditional energy resources such as solar and wind (with others) as well as energy storage devices. Most of these are grid-connected via power-electronic converters specifically inverters and rectifiers instead of spinning mechanical machines.

As of today, most of the inverter-based resources (IBRs) are connected via a grid-following (GFL) type of inverter control that follows the grid voltage and frequency to inject a specific amount of active and reactive power. The primary assumption of the GFL type of control is that the majority of the power generation still comes from fossil fuel-based SGs which keeps the grid stiff and strong which is not the case today. As more and more renewables are being deployed into the transmission and distribution networks, it becomes a challenge to keep the grid strong due to the lack of inertial response, fault ride-throughs, reactive power control, and other factors that IBRs (especially GFL type) can not offer.

One of the possible solutions to increase the penetration of more renewable power sources into the grid is the grid-forming (GFM) inverters. GFMs are voltage source inverters capable of operating and maintaining stable grid voltage levels even in a weak grid. Moreover, these inverters must have capabilities such as black-start during black-out events, providing better frequency response, virtual inertial response, fault ride-through, etc for a stable IBR-dominated power grid. The mission of the grid-forming inverters is not to replicate the synchronous generator as this could compromise some of the superior functionalities that IBRs offer. Instead, the goal is to enhance the inverter's capabilities by incorporating the synchronous response from the generators besides contributing positively to the grid stability.

The control topology in any inverter impacts the stability, resiliency, and performance of the system. There are numerous control strategies proposed in the literature that are related to grid-forming inverters. Essentially, most of the control strategies try to replicate or integrate the synchronous generator's response in IBRs. Two of the major control strategies of synchronous machines, droop control, and swing equation-based control are recognized by researchers and implemented in the field. This research includes a brief discussion on the duality between grid-following and grid-forming inverters. Following the duality theory, an enhancement in droop control is also proposed, that can emulate the synchronous generators' swing characteristics and droop control within the same control loop. This advancement improves overall system robustness and performance compared with traditional droop control. The control methodology is also verified using MATLAB simulations. A controller hardware-in-loop experiment is also carried out to verify the claims under practical situations.

1.1 Organization of Thesis

Chapter 2 provides a comprehensive literature review and key research contributions. In chapter 3, an overview of the mathematical modeling of a synchronous generator with its major control strategies is discussed. Chapter 4 compares the current grid-following inverters, with the grid-forming inverters from a perspective of synchronizing loops, grid interface, and small signal models. Chapter 5 outlines traditional control approaches of grid-forming inverters presented in the literature, and an enhanced droop control is also proposed. The mathematical analysis, performance overview, and comparison with traditional controls are obtained using bode-plot analysis, small signal stability, eigenvalue analysis, and step response. The proposed droop control is verified using SIMULINK simulations, and the results are briefly discussed in chapter 6. Moreover, hardware tests using controller hardware-in-loop are performed to verify the effectiveness of the control. Finally, Chapter 8 concludes the thesis and proposes some shortcomings of the control that need to be addressed in future work.

CHAPTER 2: LITERATURE REVIEW

The two elegant GFM control techniques proposed in the literature are droop control [2] and Virtual Synchronous Generator (VSG) [3]. The droop control is a well-established and famous grid-forming control technique due to its simplicity, flexibility, decentralized controllability, and reliability. [4], [5], [6], [7].

The operating principle of a droop-based controller evolved after conventional power plants and the integration of these plants into the grid. Droop control is based on a linear co-relationship between active power-frequency $(P-f)$ and reactive power-voltage $(Q-v)$. The droop control also enables the power-sharing between decentralized resources to meet the total demand. Several modifications were also proposed in the literature to improve the stability and resiliency of the droop control. This literature [8], [9] includes adding a differentiator to droop equations and a virtual impedance loop accordingly to improve the transient response & power sharing.

VSG control emulates the dynamics of a synchronous generator using the swing equation characteristics and provides virtual inertia. However, the major difference between different literature is the depth of the swing Equation [3], [10]. There are many more advancements in VSG control as well and some of them are hybrid types of controllers with VSG and droop control. The literature [11] proposes a hybrid control loop SME-EDC where, along with synchronous machine loop, frequency-active power, and voltage-reactive power droop loops are also embedded to provide dynamic frequency response by providing the frequency & voltage references during black start.

Apart from these major contributions, there are multiple proposals as well where different dynamics of synchronous generators are implemented [1], [12], [13], [14]. In summary, the advancements in GFMs highlight their potential to replace conventional fossil fuel-based power generation with renewable energy-based power generation ensuring stability and maintaining the grid resiliency.

2.1 Key Research Contributions

Key contributions of this research are as follows:

1. A comparative analysis between grid-following inverters (GFL) and grid-forming inverters (GFM) with the duality theory approach. (Chapter -4).

2. Stability and similarity analysis of three different GFM controls i.e. droop control, VSG control, and SME-EDC control. An improved droop control is also proposed which has integrated synchronous generator's dynamics. Stability and small signal analysis are performed to compare with existing control methodologies. (Chapter-5).

3. SIMULINK simulations and Hardware-In-Loop testings are performed to show the effectiveness of the proposed droop control. (Chapter- 6).

CHAPTER 3: OVERVIEW OF CONVENTIONAL SYNCHRONOUS GENERATOR

Synchronous generators, also known as alternators, are essential devices in the generation of electrical power. Typically, SG is a type of synchronous machine that converts mechanical energy from prime movers into controlled electrical energy. A synchronous generator contains two major components: a rotor and a stator.

The rotor carries a magnetic field and the stator consists of the armature windings also referred to as stator winding. The prime mover provides mechanical power to the rotor, which results in flux linkage in the stator windings. Thus, the electrical power is generated using Faraday's law. This electrical power is regulated and controlled using different controls available in SG such as droop control, excitation control, AGC, etc...

Section 3.1 gives an overview of the operating principle of the synchronous generator, starting with the basics of Faraday's laws with an example of a coin rotating in the magnetic field. Section 3.2 outlines the mathematical expressions of induced EMF and the voltage at the terminals of the generator. Following the EMF generation, sections 3.3 and 3.4 outline the equivalent circuit and swing dynamic equation of the synchronous generator accordingly. Sections 3.5.1 and 3.5.2 summarise two of the control systems that are essential in a synchronous generator's stable and reliable operation.

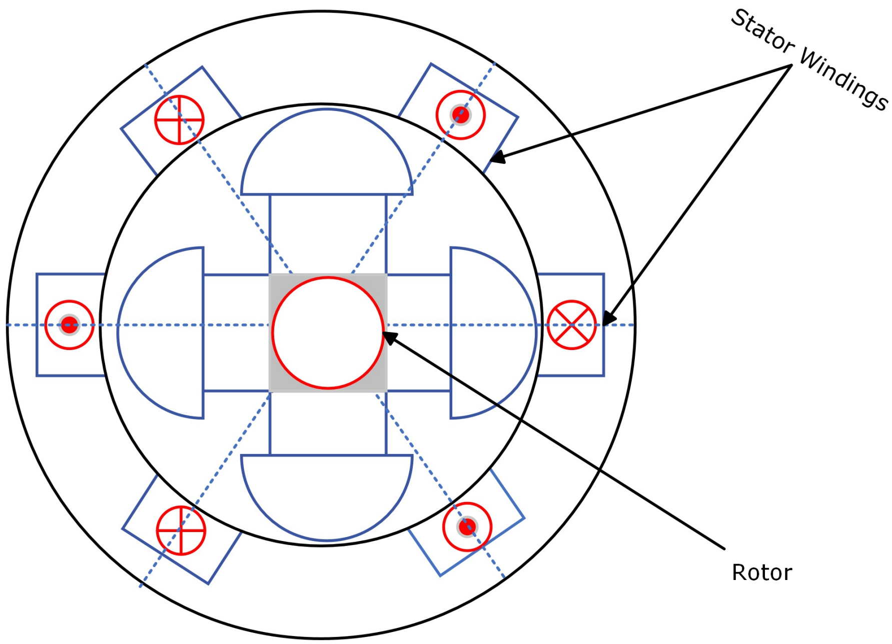

Figure 3.1: Cross-section view of SG

3.1 Operating Principle of Synchronous Generator

As mentioned earlier, SG operates based on Faraday's law. To visualize this, consider a scenario where a magnetic field is generated by the North (N) and South (S) poles as illustrated in Fig. 3.2.

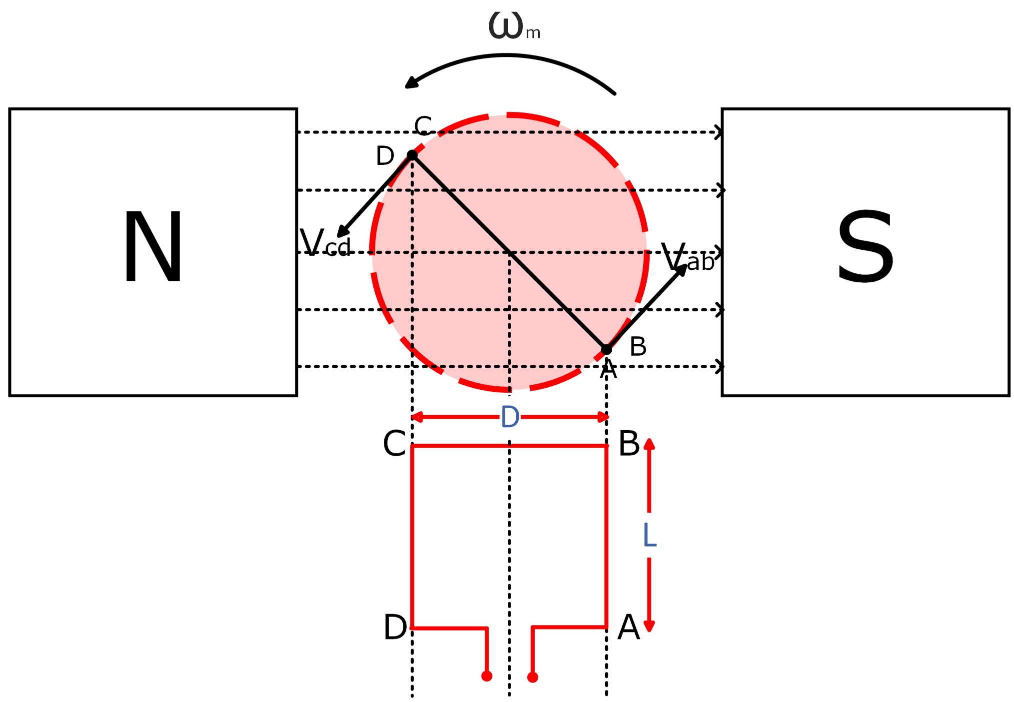

Figure 3.2: A coil rotating in a magnetic field

Now consider a spinning coil in between this magnetic field, which is cutting across the magnetic flux of NS poles. Consider a coil labeled $ABCD$, rotating within the magnetic field produced by NS as shown in Fig. 3.2. As this coil spins within a concentrated magnetic field, it experiences a dynamic change in magnetic flux due to angular motion. According to Faraday's law of EMI, this flux change induces the EMF within the coil.

$$\varepsilon = -\frac{d\phi}{dt} \tag{3.1}$$

Where: $\varepsilon =$ the induced EMF, $\phi =$ the magnetic flux through the coil, t= time.

The flux linkage to the coil can be expressed as:

$$\phi = B \cdot A \cdot \cos(\Theta) \tag{3.2}$$

$$A = D \cdot L \tag{3.3}$$

Where: B is magnetic field strength, A is the cross-sectional area of the coil, Θ = angle between the magnetic field and the axis normal of the coil. From Equations 3.1, and 3.2 the EMF in the rotating coil is directly proportional to the rate of change of the magnetic flux. So, when the prime mover powers up the rotor, it changes the magnetic field and hence the EMF is generated.

3.2 Induced EMF in Synchronous Generator

As mentioned in Equation 3.2, the flux is in the form of a sinusoidal waveform, which results in AC voltage at the terminal of the generator. This voltage has a specific frequency associated with it and can be expressed as Equation 3.4.

$$f_e = \frac{N_s \cdot P}{120} \tag{3.4}$$

Where: f_e = electrical frequency, N_s = synchronous speed of the rotor, P = number of poles.

Since the frequency of the electrical grid is constant, it is mandatory to keep the electrical frequency (f_e) constant at the terminal of the generator as well, which results in a constant mechanical rotation speed (N_s). There is a control system to keep track of the frequency and active power as mentioned in section 3.5.

$$B = B_m \cdot sin(\omega_m t) \tag{3.5}$$

By taking the average over $[0, \pi]$ of Equation 3.5, we get

$$B_{avg} = \frac{2 \cdot B_m}{\pi} \tag{3.6}$$

From equation 3.4, the average flux per pole will be:

$$\Phi_m = B_{avg} \cdot A_{perpole} \tag{3.7}$$

Substituting the value of B_{avg},

$$\Phi_m = \frac{2 \cdot B_m \cdot D \cdot L}{p \cdot \pi} \tag{3.8}$$

So, from Equation 3.4,

$$\Phi = \Phi_m \cdot \cos(\omega_m \cdot t) \tag{3.9}$$

Where, $\Phi_m = \frac{2 \cdot B_m \cdot D \cdot L}{p \cdot \pi}$

From the theorem of electromagnetic induction, the generated emf is equivalent to a change of flux per turn. So, for N turns:

$$e = -N \cdot \frac{d\phi}{dt} \tag{3.10}$$

$$e = -N \cdot \frac{d(\phi_m \cdot \cos(\omega_m \cdot t))}{dt} \tag{3.11}$$

$$e = N \cdot \phi_m \cdot \omega_m \cdot \sin(\omega \cdot t) \tag{3.12}$$

By taking the Root-Mean-Square (RMS) value of 3.12, we get

$$e_{rms} = \frac{N \cdot \phi_m \cdot \omega_m}{\sqrt{2}} \tag{3.13}$$

By replacing the values of $\omega_m = 2 \cdot \pi \cdot f_e$,

$$e_{rms} = \frac{N \cdot \phi_m \cdot 2 \cdot \pi \cdot f_e}{\sqrt{2}} \tag{3.14}$$

$$e_{rms} = N \cdot \phi_m \cdot \sqrt{2} \cdot \pi \cdot f_e \tag{3.15}$$

$$e_{rms} = 4.44 \cdot f_e \cdot N \cdot \phi_m \tag{3.16}$$

Where, e =internally generated voltage, f =frequency of generated voltage $N =$ number of turns in each stator winding phase, $\phi_m =$ magnetic flux.

3.3 Equivalent Circuit of Synchronous Generator

The internally generated voltage in a single phase of an alternator (e) is not usually the voltage at the terminal of the generator (V_t). It becomes equal only when there is no armature current in the machine which is not the case. The major reasons for this voltage drop are the self-inductance of the armature, the resistance of the coils, and the armature reaction. To incorporate the stator inductance and the self-inductance, an impedance X_L and resistance r_a are connected to complete the equivalent circuit as shown in 3.3

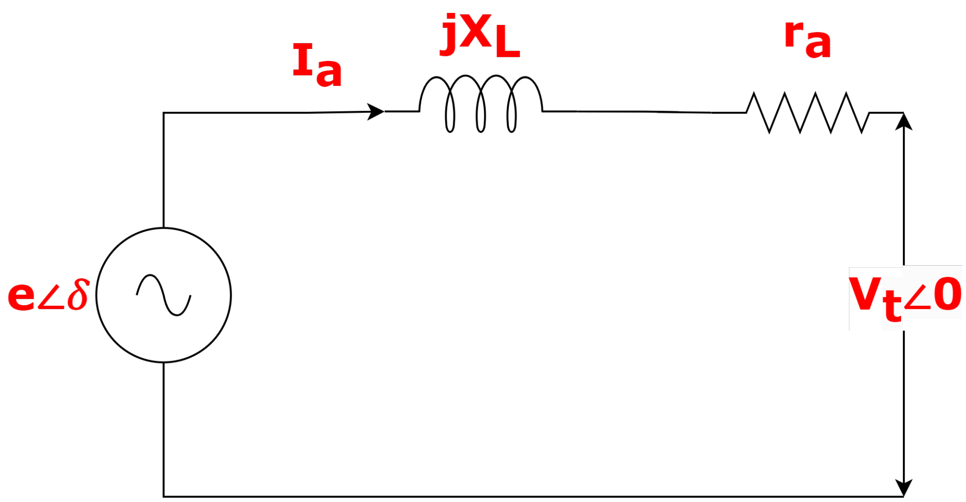

Figure 3.3: Equivalent circuit of synchronous generator

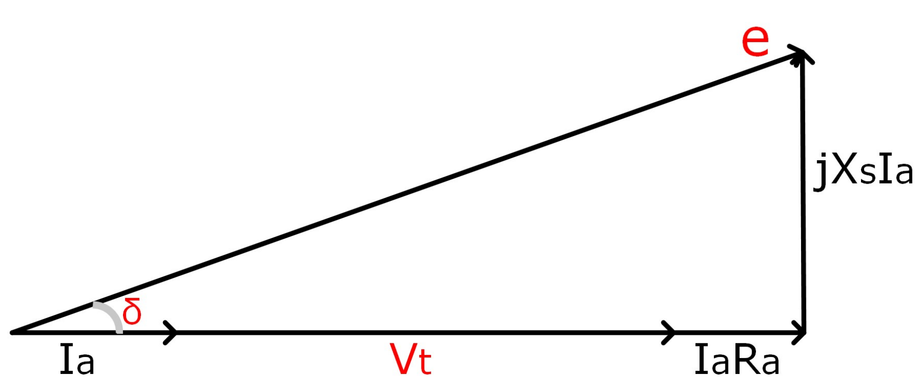

Figure 3.4: Phasor diagram of synchronous generator (unity power factor)

From the phasor diagram and equivalent circuit mentioned in figure 3.4 and 3.3, the mathematical expression of V_t will be:

$$V_t \angle 0 = e \angle \delta - I_a \cdot r_a - I_a \cdot X_L \tag{3.17}$$

3.4 Swing Equation

the dynamic behavior of a synchronous generator under steady state and transient conditions can be described by swing equations. By modeling the rotor's dynamics the swing equations provide insight into angular position and speed deviation. This relationship is also helpful in developing the control methodology for synchronous generators.

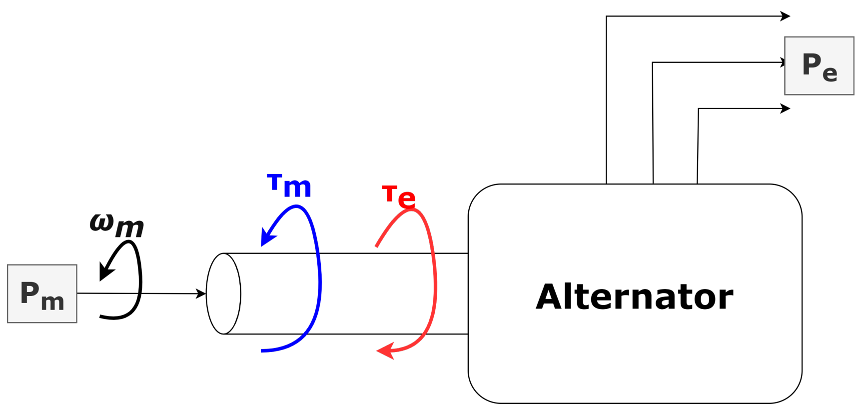

Figure 3.5: Block diagram of synchronous generator

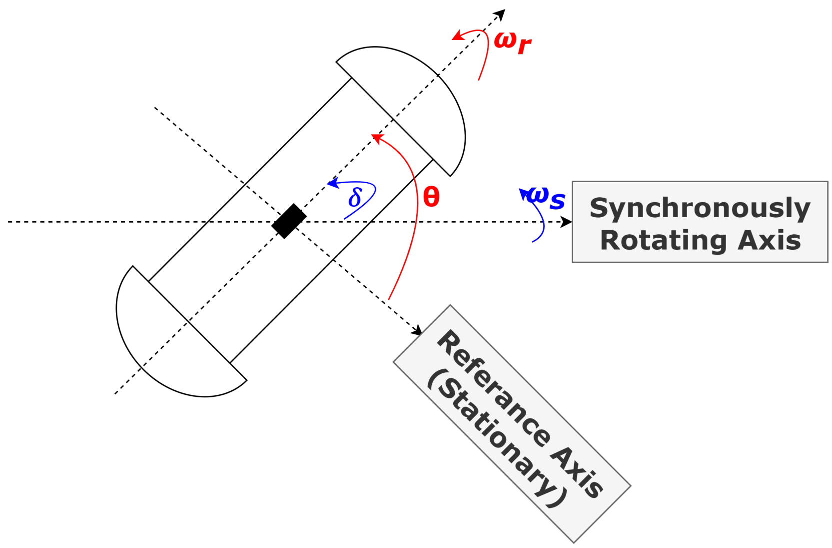

Figure 3.6: Rotor-pole representation of synchronous generator

As illustrated in figures 3.6 and 3.5, there are two torques present in the machine which are:

Mechanical Torque: Whenever the prime mover starts rotating the rotor, there is a magnetic field generated due to the interaction of the excitation system, rotor magnets and stator coils. This change of magnetic field creates a force and results in mechanical torque. This torque can be formulated as:

$$\tau_m = \frac{P_m}{\omega_m} \tag{3.18}$$

Electric Torque: The electrical torque is generated by the internally generated voltage (e). Whenever the load is connected to the synchronous generator, there will be an exchange of power (P_e) from the synchronous generator to the load. This electric power helps derive the electrical torque (τ_e). This can be formulated as:

$$\tau_e = \frac{P_e}{\omega_m} \tag{3.19}$$

Usually, there is a balance between τ_m and τ_e but during the load changes or mechanical power changes there is an accelerating torque τ_a present which changes the synchronism. τ_a is defined in Equation 3.20

$$\tau_a = \tau_m - \tau_e \tag{3.20}$$

By multiplying with ω_r which is the speed on the prime mover, we get:

$$\tau_a \cdot \omega_m = \tau_m \cdot \omega_m - \tau_e \cdot \omega_m \tag{3.21}$$

$$P_a = P_m - P_e \tag{3.22}$$

Here, the friction and windage torque is neglected.

$$P_a = \tau_a \cdot \omega_m \tag{3.23}$$

$$P_a = \tau_a \cdot \omega_m \tag{3.24}$$

$$P_a = I \cdot \alpha \cdot \omega_m \tag{3.25}$$

Where, I = moment of inertia, α = angular acceleration ($\tau_a = I \cdot \alpha$).

$$P_a = I \cdot \omega_m \cdot \alpha \tag{3.26}$$

Let,

$$M = I \cdot \omega_m \tag{3.27}$$

Where, M= angular momentum/ inertia constant.

$$P_a = M \cdot \alpha \tag{3.28}$$

Revisit the Fig.3.6,

$$\theta = \omega_m \cdot t + \delta \tag{3.29}$$

By differentiating twice on both of the sides with respect to time,

$$\frac{d\theta}{dt} = \omega_m + \frac{d\delta}{dt} \tag{3.30}$$

$$\alpha = \frac{d^2\theta}{dt^2} = \frac{d^2\delta}{dt^2} \tag{3.31}$$

$$P_a = M \cdot \frac{d^2\theta}{dt^2} = M \cdot \frac{d^2\delta}{dt^2} \tag{3.32}$$

The Equation 3.32 is known as the swing equation. This equation can be derived in mechanical parameters as shown below:

$$\tau_a = \tau_m - \tau_e \tag{3.33}$$

$$\tau_m - \tau_e = J \cdot \alpha \tag{3.34}$$

$$\tau_m - \tau_e = J \cdot \frac{d^2\theta}{dt^2} \tag{3.35}$$

Where, J = Inertial constant in mechanical domain. The above equation is also the swing equation but in the mechanical domain. The physical significance of J, M, and H can be derived from kinetic energy as below:

$$\text{K.E.} = \text{Kinetic Energy} = \frac{1}{2} \cdot I \cdot \omega_m^2 \tag{3.36}$$

As mentioned above, $M = I \cdot \omega_m$, So,

$$\text{K.E.} = \text{Kinetic Energy} = \frac{1}{2} \cdot I \cdot \omega_m^2 = \frac{1}{2} M \cdot \omega_m \tag{3.37}$$

By converting the mechanical domain into the electrical domain by using the ω_m and ω_e formula, we get,

$$M = \left(\frac{2}{p}\right)^2 \cdot I \cdot \omega_e \tag{3.38}$$

Let's define a term, $H = \frac{\text{Stored Kinetic Energy at Synchronous Speed (K.E.)}}{\text{MVA Rating of the machine}(G)}$. This term is useful for finding a new constant related to the moment of inertia but in the electrical domain.

$$\text{K.E.} = G \cdot H \tag{3.39}$$

$$\frac{1}{2} \cdot M \cdot \omega_m = G \cdot H \tag{3.40}$$

$$M = \frac{2 \cdot G \cdot H}{\omega_m} \text{(Mechanical Domain)} \tag{3.41}$$

$$M = \frac{G \cdot H}{\pi \cdot f_e} \text{(Electrical Domain)} \tag{3.42}$$

3.5 Control of Synchronous Generator

Achieving stable power system operation involves maintaining constant frequency and voltage, along with providing the required amount of active and reactive power to the load. Active power can be controlled by changing the mechanical input to the machine, while reactive power can be controlled using changing the excitation of the machine.

As mentioned in Fig. 3.7, there are typically two controls: frequency-power droop (AGC) and voltage-reactive power droop (AQC) also referred to as excitation system control. These control systems control the active and reactive power by regulating AC frequency and voltage accordingly. These control systems are modeled individually in section 3.5.1 and 3.5.2.

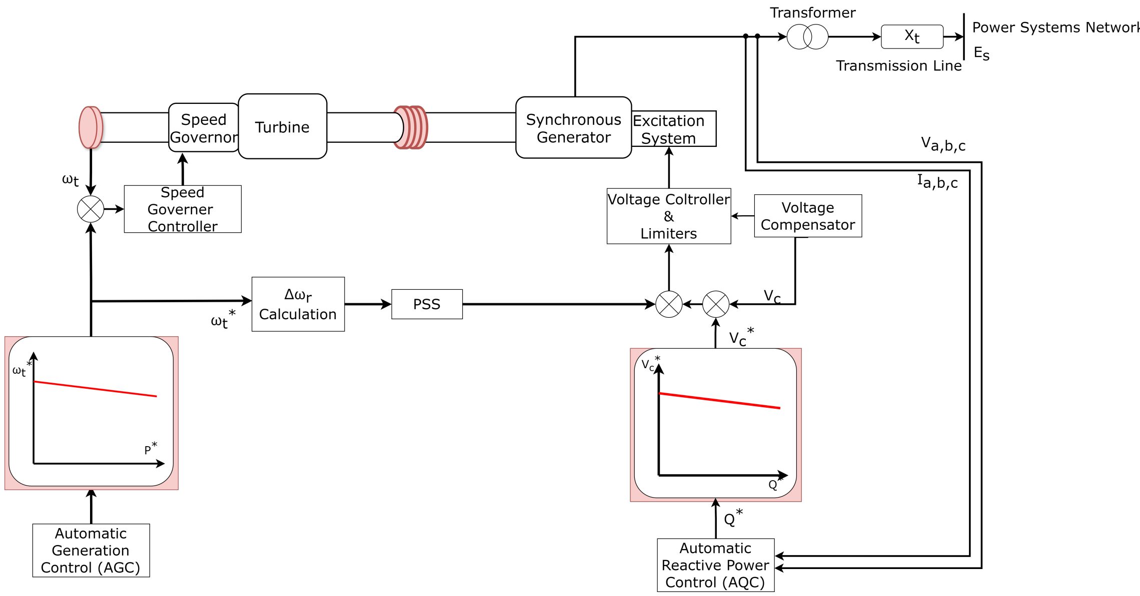

Figure 3.7: Block diagram of synchronous generator control

3.5.1 Active Power- Frequency Droop/ Automatic Generation Control

The motive of active power-frequency droop control is to regulate the AC frequency and control the active power flow from the synchronous machine to the grid. To model this control, let's consider an isolated synchronous generator (SG) with a rigid shaft system and its load as shown in Fig. 3.8. Since there is only one generator, not multiple, the speed governing equation can be referred to from section 3.4, Equation 3.32.

$$2 \cdot H \cdot \frac{d\omega_m}{dt} = \tau_m - \tau_e \tag{3.43}$$

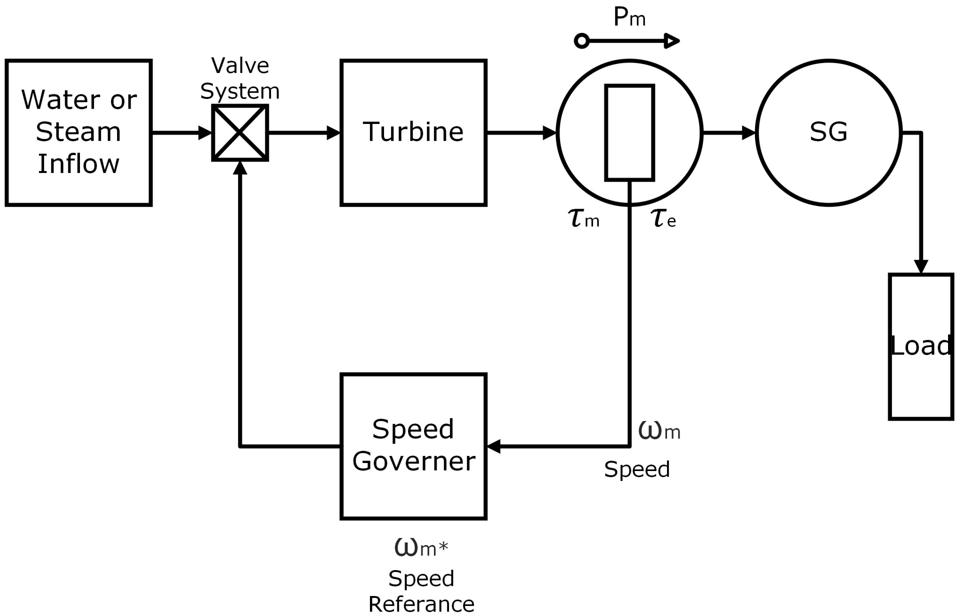

Figure 3.8: Synchronous generator with local load

The power can also be represented as torque, by incorporating ω_m.

$$P_m = \omega_0 \cdot \tau_m \tag{3.44}$$

Let's consider a small change (Δ) in torque and speed,

$$\tau_m = \tau_{m0} + \Delta T_m \tag{3.45}$$

$$\tau_e = \tau_{e0} + \Delta \tau_e \tag{3.46}$$

$$\omega_m = \omega_0 + \Delta \omega_m \tag{3.47}$$

During the steady state, the $\tau_{m0} = \tau_{e0}$, So the above equations will be modified as:

$$\Delta P_m - \Delta P_e = \omega_0(\Delta \tau_m - \Delta \tau_e) \tag{3.48}$$

From Equation 3.32,

$$2 \cdot H \cdot \frac{d\Delta\omega_m}{dt} = \frac{(\Delta P_m - \Delta P_e)}{\omega_0} \tag{3.49}$$

$$M = 2 \cdot H \cdot \omega_0 \tag{3.50}$$

To add the damping effect, a new term $D \cdot \Delta\omega_m$ is added with ΔP_L which is equivalent to ΔP_e,

$$\Delta P_e = \Delta P_L + D \cdot \Delta\omega_m \tag{3.51}$$

Where, ΔP_L = the load power change, D = damping constant for the frequency-power droop. The above equation can be re-written as:

$$2 \cdot H \cdot \omega_0 \cdot \frac{d\Delta\omega_m}{dt} + D \cdot \Delta\omega_m = \Delta P_m - \Delta P_L \tag{3.52}$$

The variations in electrical load are directly related to the changes in $\Delta\omega_m$ and according to the controller sensitivity, these changes affect the system stability. In case of a sudden step change in the load power (ΔP_L), the resulting speed can be derived by: $\Delta\omega_m = \frac{\Delta P_L}{D}$. This error can be controlled using a simple integrator controller, which drives the system toward the nominal speed as shown in Fig. 3.9. This control is an isochronous speed-governor control which is useful to control standalone generators, not multiple generators since load sharing needs to be incorporated.

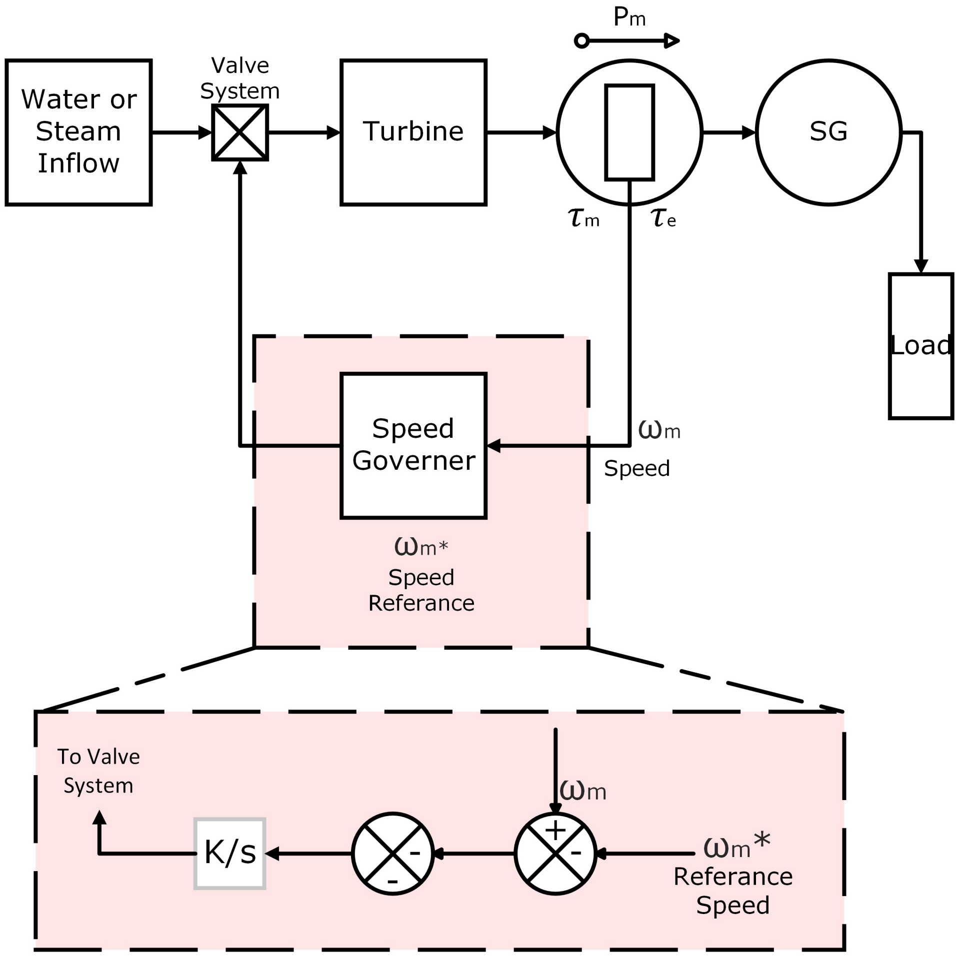

Figure 3.9: Speed-droop control for isochronous generator

Since this control does not include load sharing when multiple generators operate in parallel, a feedback loop is added with a gain (R) (Equation 3.53) as shown in Fig. 3.10.

$$R = \frac{-\Delta f}{\Delta P_L} \tag{3.53}$$

With two (or more) alternators connected in parallel, the frequency will be the same for all of them, thus the load sharing depends on their speed-droop response. Hence,

$$-\Delta P_1 R_1 = \Delta f \tag{3.54}$$

$$-\Delta P_2 R_2 = \Delta f \tag{3.55}$$

which results in,

$$\frac{\Delta P_2}{\Delta P_1} = \frac{R_1}{R_2} \tag{3.56}$$

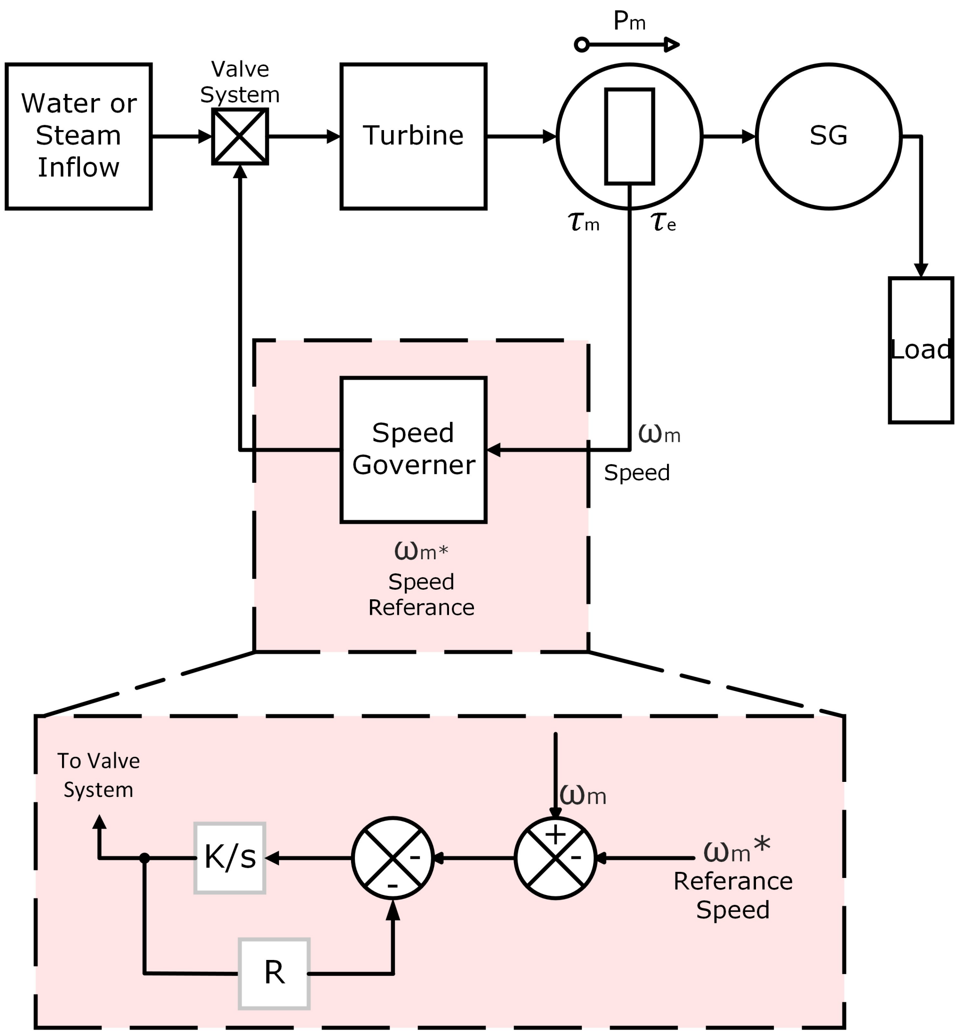

Figure 3.10: Power transfer function with load frequency component

Whenever the speed droop is identical, $(R_1 = R_2)$, the two alternators' load change is proportional to their changes. The speed/load response can be adjusted by the load reference point. Changing the reference point vertically affects the power delivered by the alternator at a given frequency as shown in Fig. 3.11. An example of the $60Hz$ frequency is mentioned above. A single alternator can deliver zero power at set-point: A, 50% power at set-point: B, and 100% power at set-point: C.

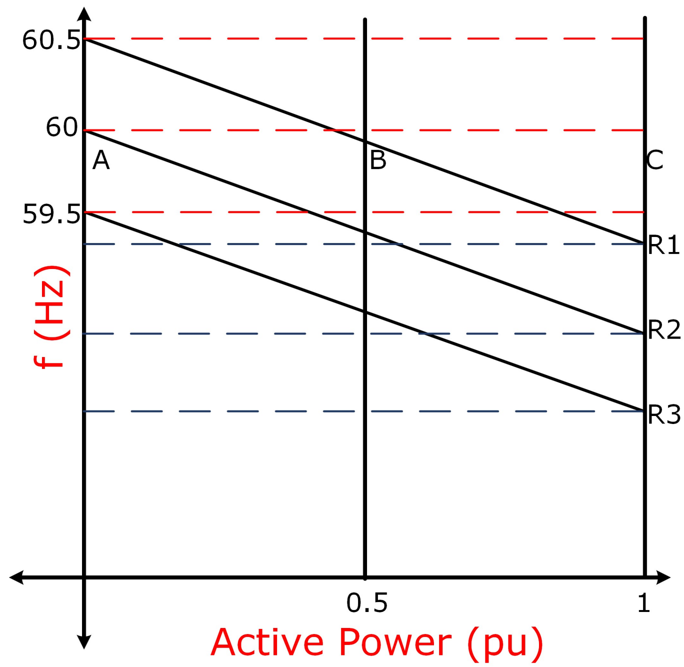

Figure 3.11: Speed-power characteristics

3.5.2 Excitation System Control

The Automatic Voltage Regulation (AVR) changes the field excitation based on the requirements of the reactive power. The AVR acts based on the error between reference reactive power, reference voltage, and current reactive power and current voltage and changes the I_f (field current) therefore, changing the internally generated voltage. So, the excitation system of SG contains $Q - V$ droop loop and the exciter to change the voltage seen by the load. There are three types of exciters present currently: (a) DC exciters, (b) AC exciters, and (c) Static exciters (power electronics based).

Typically, the static exciter is configured from a three-phase rectifier with its control to produce the V_f. This rectifier is fed with the AC voltage source of voltage V_{ex} and provides I_f load current. This controlled current is fed to the field windings. As shown in Fig. 3.7, the $Q - V$ will lead to the reference voltage V_c^*. The measured voltage V_G is calculated from an impedance voltage droop, to obtain the compensated voltage. Then the error $V_c^* - V_c$ enters the excitation system, and from the controls of the exciter the I_f is generated. Fig. 3.12 is the static exciter block diagram, where V_{ex} is the input AC voltage to the 3-phase rectifier and it gives controlled I_f as a load output current.

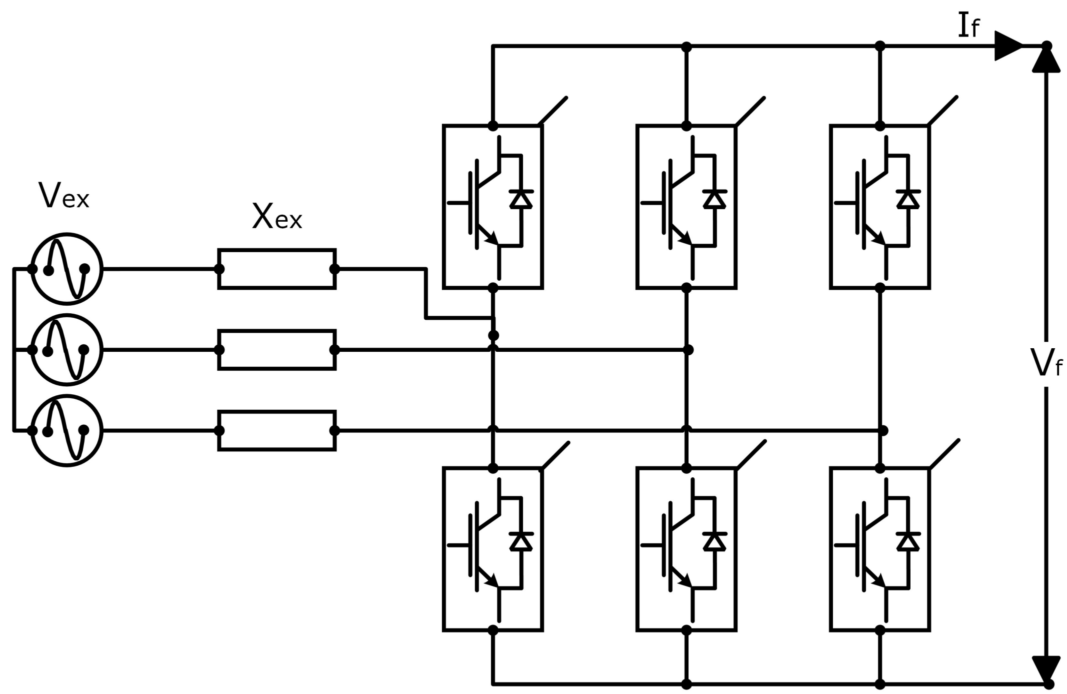

Figure 3.12: Static exciter 3-phase rectifier

CHAPTER 4: GRID FOLLOWING AND GRID FORMING INVERTERS

Power electronic converters used for IBRs are normally classified into two categories: (a) Grid-Following (GFL) and (b) Grid-Forming (GFM). A grid-following inverter controls its AC-side current and follows the phase angle of existing grid voltage through a phase-locked loop (PLL). On the other end, the grid-forming inverter controls the AC-side voltage and forms a voltage-sourced grid. It has several droop loops which helps synchronization with the weak grid or other inverters. The grid-following inverters are widely used due to their simple control structure, mature PLL loop, and the feature of current control. However, PLL has some negative effects while the inverter is operating with a weak grid. This instability makes the entire system unstable if the grid is IBR-dominated and may cause system collapse. These issues in GFL can be solved using GFM inverters, and novel control strategies.

This chapter outlines the key differences or similarities between the GFLs and GFMs. Section 4.1 reviews the nature of the grid following and grid forming inverters. After the overview of the current source and voltage source inverters, section 4.2 and 4.3 outlines the key similarities between synchronizing loops and their small signal stability accordingly.

4.1 Current Source V/s Voltage Source Inverter

As mentioned earlier, the GFL inverter takes the reference phase angle, and voltage from the existing grid, and forms a current reference to inject specified power into the grid. Whereas, the GFM inverters form the reference voltage to form a stable grid. In other words, the grid-following and grid-forming inverters are more accurately voltage-following and voltage-forming accordingly. In addition to this, the power control of the grid following the inverter implies that it is current forming, and the power-frequency droop of GFM implies that GFMs are current following. So, the grid following and grid forming inverters can be more precisely redefined as: *Voltage following, Current forming* and *Current following, Voltage forming.* Alternatively, the grid-following inverters are the Thevenin equivalent of grid forming, and grid-forming inverters are the Nortan's equivalent of grid following.

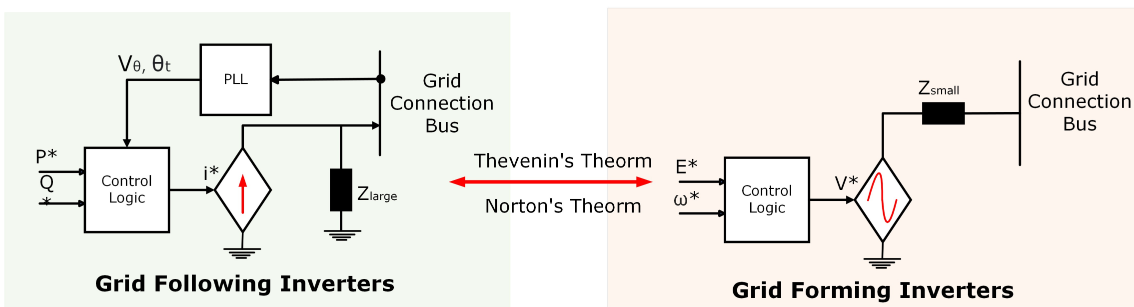

Figure 4.1: Transformation between grid following and grid forming inverters.

4.2 Synchronizing Loops

The block diagram of the generalized control structure of GFL and GFM is shown in Fig.: 4.2. The highlighted control blocks are the synchronizing loops in the respective inverter *(i.e. PLL and current controller for GFL & Frequency-power droop and voltage controller for GFM.)*

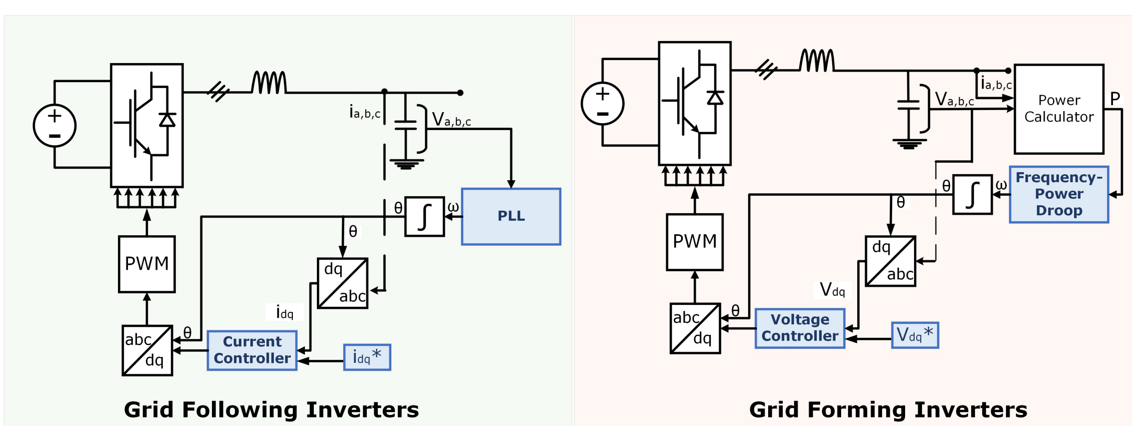

Figure 4.2: Grid following and grid forming inverter's control structure in d-q reference frame.

As shown in Fig.4.2, the synchronizing loop in GFL consists of a PLL, and on the other end, GFM does have a $P-f$ droop. These loops have similar structures, but instead of current in GFL, the voltage in GFM is controlled. This similarity is shown in Fig.4.3.

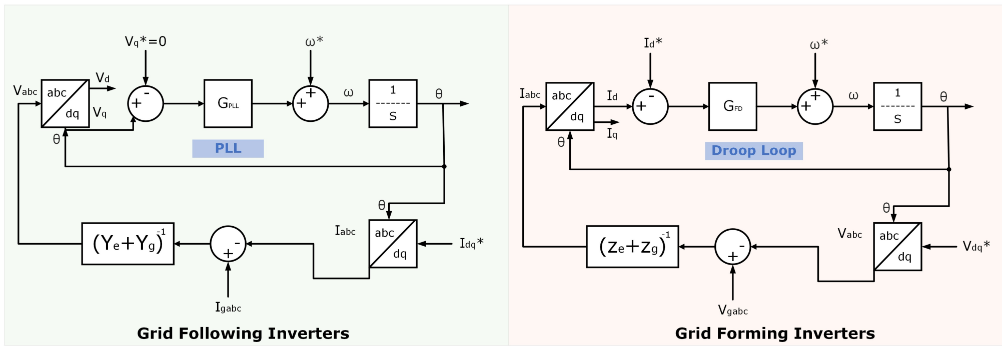

Figure 4.3: Grid following and grid forming inverter's synchronizing loops.

The G_{PLL} and G_{FD} also have similar structures consisting of a linear gain and a low-pass filter. But the only difference between those is that the G_{FD} is a linear controller, whereas F_{PLL} is a PI controller with integral which quantitatively proves that there will be some steady-state error with GFM which will be also mentioned in Chapter- 5. By comparing the synchronizing loops, it is embedded that the swing characteristics of PLL and $P-f$ loop also have a similar structure, with a duality of *current control in GFL* and *voltage control in GFM.*

4.3 Small Signal Stability

The swing of PLL-based grid-following is unclear and undefined. On the other hand, it has been said that the frequency droop grid-forming inverter control behaves similarly to a virtual synchronous generator control (VSG) [7, 6] and which will be also proven in chapter 5.

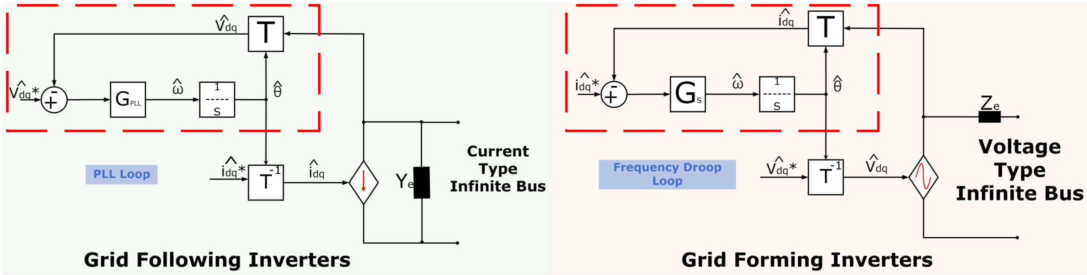

Figure 4.4: Transformation between grid following and grid forming inverters.

The synchronizing loop for the PLL-based grid following inverters is as mentioned in 4.3, and its small signal model in $dq\pm$ frame is shown in Fig. 4.4. The grid-following inverter is modeled by a controlled current source embedded with voltage-following and current-forming features. The admittance Y_e represents the effective admittance of the AC filter and inner current loop [15, 16]. From Fig. 4.4, the PLL equation can be written as:

$$\omega = \omega^* + G_{PLL}(V_q - V_q^*) \tag{4.1}$$

$$\theta = \frac{1}{s} \cdot \omega \tag{4.2}$$

Small signal loop equation can be written as:

$$\hat{\omega} = G_{PLL} \cdot \frac{\hat{V_+} - \hat{V_-}}{2 \cdot j} \tag{4.3}$$

$$\hat{\omega} = \frac{1}{2 \cdot j} \cdot G_{PLL} \cdot [1 - 1] \cdot \begin{bmatrix} \hat{v_+} \\ \hat{v_-} \end{bmatrix} \tag{4.4}$$

$$\hat{\theta} = \frac{1}{s} \cdot \hat{\omega} = \frac{1}{s} \cdot G_s \cdot \hat{v_{dq}} \tag{4.5}$$

PLL admittance can be represented as:

$$Y_{PLL} = \frac{1}{2S_{v\theta}} \cdot \begin{bmatrix} I_{+0} & -I_{+0} \\ -I_{-0} & I_{-0} \end{bmatrix} \tag{4.6}$$

The whole system can be modeled as:

$$Y_t^{-1} = (Y_{PLL} + Y_g)^{-1} = Y_g^{-1}(S'_{v\theta})^{-1} \tag{4.7}$$

Alternatively, the synchronizing loop for the droop-based GFMs is also shown in 4.3, and its small signal model in dq frame is shown in Fig. 4.4. The grid-forming inverter is modeled by a controlled voltage source embedded with a current-following and voltage-forming feature. Since the grid-forming inverter is voltage-sourced, it has to be represented with a series impedance Z_e.

From Fig. 4.4,

The PLL equation will be:

$$\omega = \omega^* + G_{FD}(i_d - i_d^*) \tag{4.8}$$

$$\theta = \frac{1}{s} \cdot \omega \tag{4.9}$$

Small signal loop equation can be written as:

$$\hat{\omega} = G_{FD} \cdot \frac{\hat{i_+} - \hat{i_-}}{2} \tag{4.10}$$

$$\hat{\omega} = \frac{1}{2} \cdot G_{FD} \cdot [1 \;\; 1] \cdot \begin{bmatrix} \hat{i_+} \\ \hat{i_-} \end{bmatrix} \tag{4.11}$$

$$\hat{\theta} = \frac{1}{s} \cdot \hat{\omega} = \frac{1}{s} \cdot G_s \cdot \hat{i_{dq}} \tag{4.12}$$

Droop admittance can be modelled as:

$$Z_{FD} = \frac{1}{2S_{i\theta}} \cdot \begin{bmatrix} jV_{+0} & jV_{+0} \\ -jV_{-0} & -jV_{-0} \end{bmatrix} \tag{4.13}$$

Whole system can be written as:

$$Z_t^{-1} = (Z_{FD} + Z_g)^{-1} = Z_g^{-1}(S'_{i\theta})^{-1} \tag{4.14}$$

Rephrasing the small signal equations, the grid-following inverter has voltage-angle swing characteristics from PLL alternatively a dual, grid-forming inverter has current-angle swing from frequency droop control.

In summary, the grid-following and grid-forming inverters have similar structures but with a duality in the control objectives [6]. The comprehensive comparison is also shown in table 4.1. So, the synchronizing loops, grid interfacing attributes, small-signal analysis, and controller gains are dual to each other but similar in construction. By looking into these features, it can be also implied that the small-signal equality and transient stability mechanisms are also similar.

Table 4.1: Grid following and grid forming inverters at a glance

	PLL based GFL	$P - f$ **Droop based GFM**
Type of inverter	Current source inverter	Voltage source inverter
Objectives	To deliver specified current (power) to the grid	Setup a stable grid voltage
Controlled quantities	AC current/power	AC voltage magnitude and frequency
Synchronizing loops	PLL loop	$f - P$ droop loop
Interaction with grid	Voltage following - current forming	Current following - Voltage forming
Mathematical relationships	$Q - \theta$	$P - \theta$
Small signal stability	$\hat{\omega} = \frac{1}{2 \cdot j} \cdot G_{PLL} \cdot [1 \ -1] \cdot \begin{bmatrix} \hat{v_+} \\ \hat{v_-} \end{bmatrix}$	$\hat{\omega} = \frac{1}{2} \cdot G_{FD} \cdot [1 \ \ 1] \cdot \begin{bmatrix} \hat{i_+} \\ \hat{i_-} \end{bmatrix}$

CHAPTER 5: CONTROL STRATEGIES FOR GRID FORMING INVERTERS

This chapter outlines different grid-forming controls especially the droop control, VSG control, and SME-EDC control. Apart from the review, a novel control loop is also proposed with its mathematical analysis and stability criteria. Section 5.1, 5.2 and 5.3 presents droop control, VSG, and SME-EDC control with a brief discussion on the block diagrams, mathematical equations, and the transfer functions. Section 5.4 proposes a novel control methodology termed "Enhanced Droop Control with Integrated Synchronous Machine Emulation (EnDC-InSME)". With the proposal of the control methodology, the mathematical formulations, and transfer functions are derived with comparison with the previous control algorithms. Section 5.5 provides the small signal stability of EnDC-InSME using eigenvalue analysis and step response.

There are numerous grid-forming inverter controls available as shown in Fig. 5.1 and even more. The Virtual Synchronous Machine based [10], Matching Control [17] and Droop based controls [2] are three of the widely used control methodologies in a grid forming inverter[1]. These controls are related to the control and swing of the synchronous generator and that satisfies the objective of grid forming inverter to provide virtual inertia and damping to the system. There are other performance requirements from GFM resources such as robust fault ride-through, positive contribution to the system stability & voltage control, black start, and ability to perform parallel operations with other GFM/GFLs.

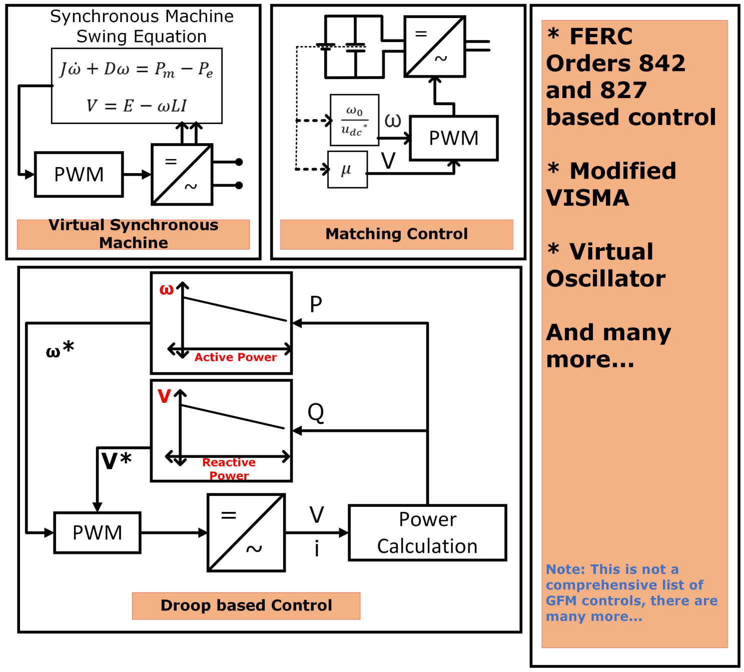

Figure 5.1: List of grid forming controls[1]

Many hybrid grid-forming controls are proposed [11, 18] to improve stability and performance, such as SME-EDC [11] where the virtual synchronous machine controller is embedded with the $P - f$ and $Q - v$ droop.

5.1 Overview of Droop Control

Droop control is one of the widely used control methods in micro-grids [2, 19], due to its simple control structure. The controller controls and regulates the AC frequency and voltage by altering the inverter's active and reactive power set-points accordingly. And these set-points are calculated from Equations 5.1 and 5.2.

$$\omega^* = \omega_0 + K_p(P_0 - P) \tag{5.1}$$

$$V^* = V_0 + K_q(Q_0 - Q) \tag{5.2}$$

Here, the ω_0 and V_0 are the constant values, and the ω^* and V^* are the reference values for the controller. And, the k_p and k_q are the droop constants.

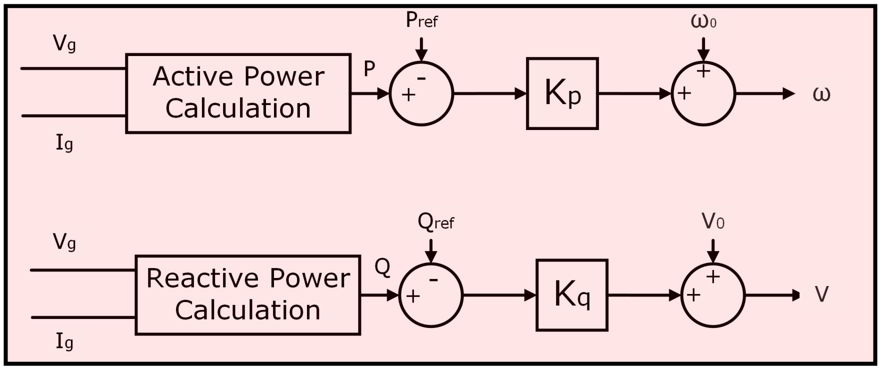

Figure 5.2: Droop control block diagram

The (ω^* and V^*) are controlled via outer voltage and current control loops. However, these controllers cannot provide virtual inertia to the inverter, which again makes the system unstable during extreme conditions.

The transfer function of the droop controller is just a constant gain ($-k_p$) as mentioned in Equation 5.3.

$$H_{\text{Droop}}(s) = \frac{\omega(s)}{P(s)} = -k_p \tag{5.3}$$

5.2 Overview of Virtual Synchronous Generator based Control (VSG)

Based on the theory of synchronous generator and the swing equation mentioned in Chapter- 3, Section -3.5, a grid forming inverter control is developed [10, 19]. These Equations- 5.4 to 5.6 are embedded in the VSG controller for grid forming controls which are also governing equations for SG.

$$e = v + iR + Ls \cdot \frac{di}{dt} \tag{5.4}$$

$$T_e = \frac{P_e}{\omega} \tag{5.5}$$

$$T_m = T_e + B \cdot \omega + J \cdot \frac{d\omega}{dt} \tag{5.6}$$

Where, J = Moment of Inertia, B = Damping factor. As shown in Fig. 5.3 and following Equation 5.6, angular frequency (ω) and phase angle (θ) are calculated from electrical output torque (T_e), mechanical torque (T_m) which is generated from the reference set point, and selected parameters J and B of synchronous generator.

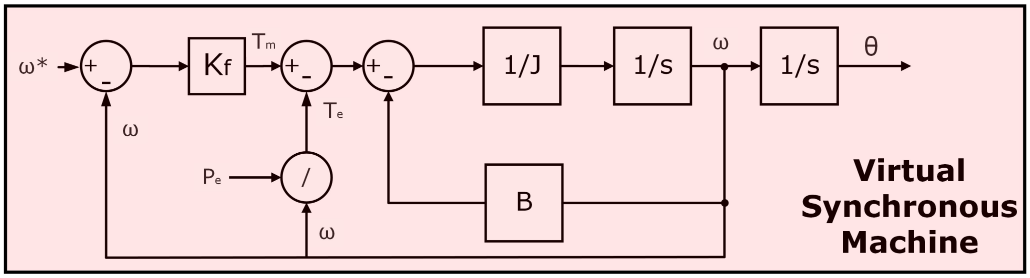

Figure 5.3: VSG control block diagram

Based on constant voltage amplitude V_g^*, and calculated θ from Equation 5.6 the reference voltages are generated. Thus, the measured voltage V_g and V_g^* are compared, and error $V_g^* - V_g$ is given to an emulated stator resistor and inductance to construct the reference current (I_{abc}^*). Since the synchronization is achieved from the VSG loop and damping effect, no PLL is required in this methodology. The transfer function can be calculated by converting the Equation 5.6 into Laplace domain as shown in 5.7:

$$T_m - T_e = B \cdot \omega + J \cdot s \cdot \omega \tag{5.7}$$

So, by ignoring the measured values (T_e), the transfer function will be:

$$H_{\text{VSG}}(s) = \frac{\omega}{T_m} \tag{5.8}$$

$$H_{\text{VSG}}(s) = \frac{\omega}{T_m} = \frac{1}{J \cdot s + B} \tag{5.9}$$

The bode plot for $H_{VISMA}(s)$ is illustrated in Fig. 5.7. This is a superior control method for the grid-forming inverter, however, during the black-start, this methodology is unable to maintain the frequency and voltage magnitude, hence a novel control loop (SME-EDC) was proposed [11].

5.3 Overview of Synchronous Machine Emulator with Embedded Droop Control (SME-EDC)

Maintaining the frequency & voltage stability requires active and reactive power control during black start and weak grid. These mechnisms can be implemented by adding droop control, as illustrated in Fig. 5.4. These droops includes: (a) the active power- frequency droop (P-f) and the reactive power-voltage droop (Q-v)[11].

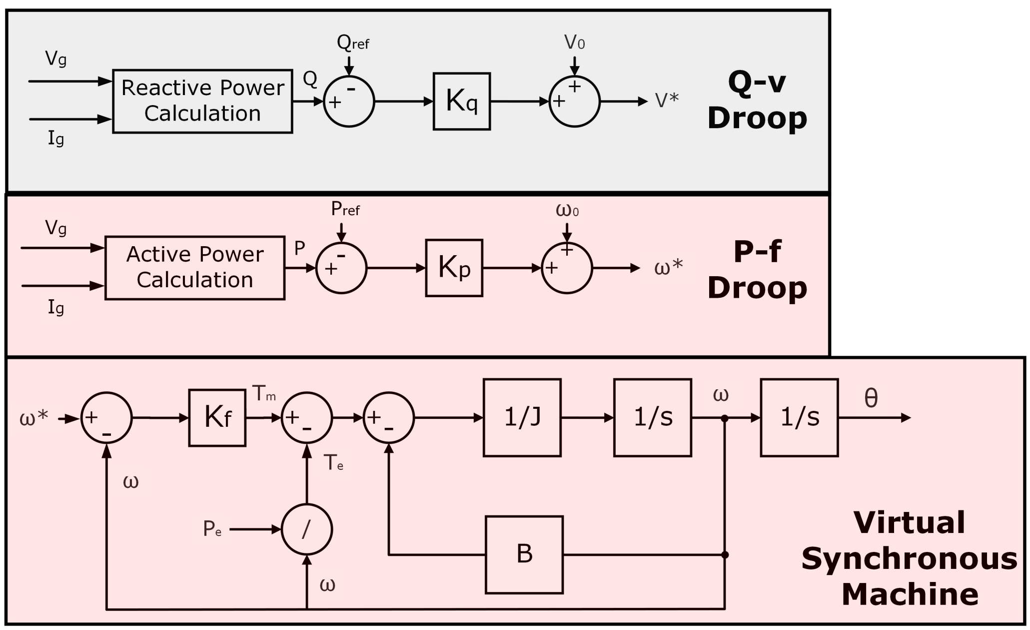

Figure 5.4: SME-EDC control block diagram

Since the droop control acts as a feedback linear gain, it can also be incorporated into the transfer function Equation 5.9, and the resultant block transfer function is illustrated in Fig. 5.5.

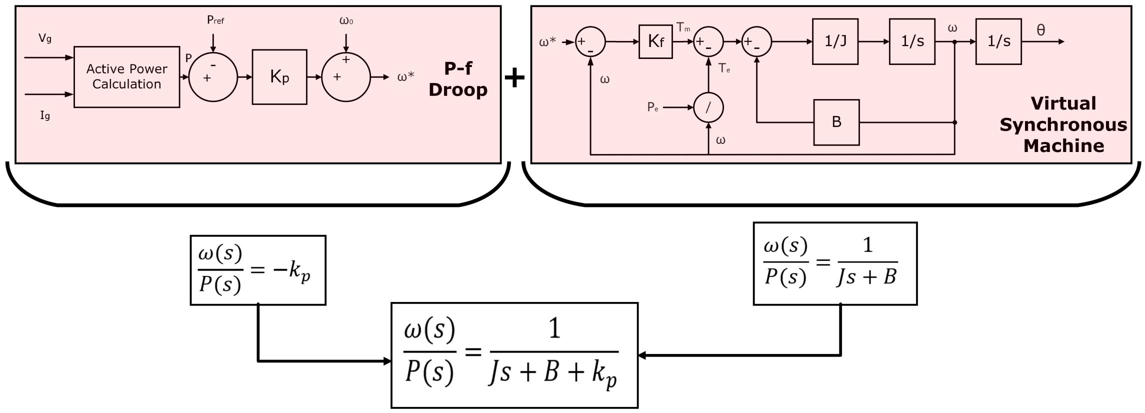

Figure 5.5: SME-EDC transfer function

The overall transfer function of SME-EDC can be obtained as:

$$H_{\text{SME-EDC}}(s) = \frac{\omega}{T_m} = \frac{1}{J \cdot s + B + k_p} \tag{5.10}$$

5.4 Enhanced Droop Control with Integrated Synchronous Machine Emulation (EnDC-InSME)

The SME-EDC control scheme comprises two primary loops: (a) the Synchronous Machine Emulator (SME) loop and (b) the P-f Droop loop. There are several proposals [7] indicating that the VSG control is quantitatively equivalent to a low pass filter's response. Hence, these loops can be seamlessly integrated by incorporating a single low-pass filter into the droop control. As shown in Fig. 5.6, the active power P_e is a measured power at the load/grid interconnection of the inverter. This P_e is low-pass filtered [7], and then the normal droop as mentioned earlier is applied. This filtering will prove necessary to emulate the synchronous generators, although their introduction is normally justified only as a solution to remove high-frequency disturbances.

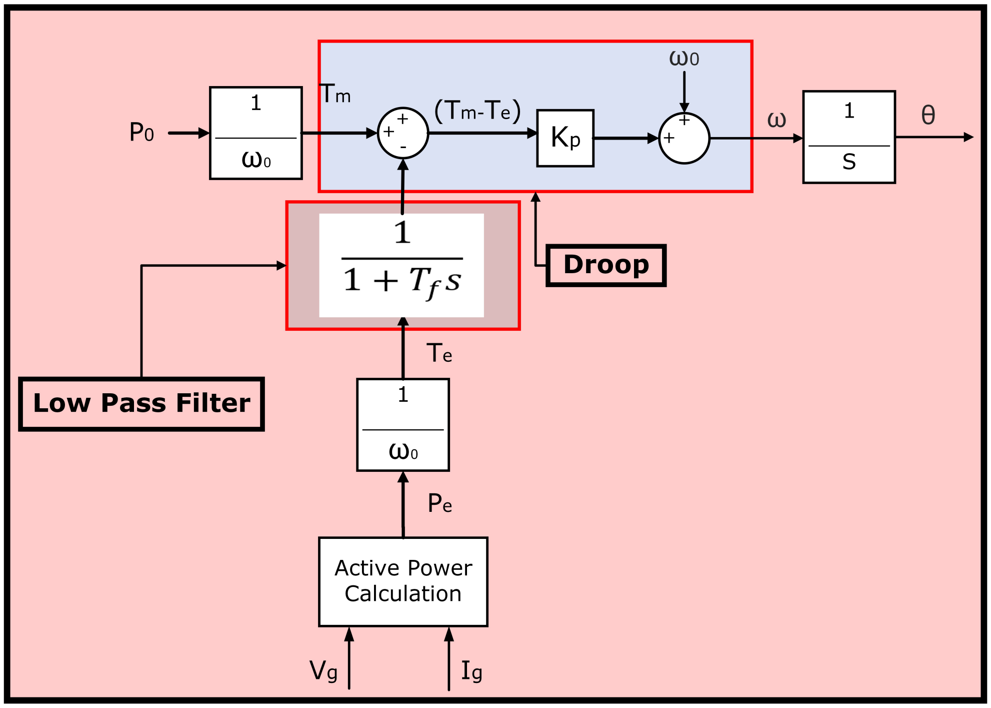

Figure 5.6: Droop control with low-pass filter block diagram

Rewriting the Equation 5.1,

$$\omega - \omega_0 = K_p \cdot \left(P_0 \cdot \frac{1}{\omega_0} - \frac{P_e}{\omega_0(1 + T_f \cdot s)} \right) \tag{5.11}$$

$$\omega - \omega_0 = K_p \cdot \left(T_m - \frac{T_e}{(1 + T_f \cdot s)} \right) \tag{5.12}$$

Where, $\frac{P_0}{\omega_0} = T_m$ and $\frac{P_e}{\omega_0} = T_e$. Rearranging this equation,

$$K_p \cdot \frac{T_e}{(1 + T_f \cdot s)} = K_p \cdot T_m + \omega_0 - \omega \tag{5.13}$$

$$\frac{T_e}{(1 + T_f \cdot s)} = T_m + \frac{\omega_0 - \omega}{K_p} \tag{5.14}$$

$$T_e = (1 + T_f \cdot s)T_m + (1 + T_f \cdot s) \left(\frac{\omega_0 - \omega}{K_p} \right) \tag{5.15}$$

$$T_e = T_m + T_f \cdot s \cdot T_m + \left(\frac{\omega_0 - \omega}{K_p}\right) + T_f \cdot s \cdot \frac{\omega_0}{K_p} - T_f \cdot s \cdot \frac{\omega}{K_p} \tag{5.16}$$

Since this is in s-domain, the $s \cdot X = \frac{dX}{dt}$, so the constant terms multiplied with s will be zero. So,

$$T_e - T_m = \frac{-\omega}{K_p} - \frac{T_f \cdot s \cdot \omega}{K_p} + \frac{\omega_0}{K_p} \tag{5.17}$$

Rearranging this equation,

$$T_m - T_e = \frac{\omega}{K_p} + \frac{T_f \cdot s \cdot \omega}{K_p} - \frac{\omega_0}{K_p} \tag{5.18}$$

Now, by comparing this equation with the VSG equation (i.e. Equation 5.6, it can be clearly said that,

$$J_{EnDC-InSME} = \text{Inertia Term} = \frac{T_f}{K_p} \tag{5.19}$$

$$B_{EnDC-InSME} = \text{Damping Term} = \frac{1}{K_p} \tag{5.20}$$

The steady-state error will be:

$$error = \frac{-\omega_0}{K_p} \tag{5.21}$$

Now, since the Equation 5.18 is already in the Laplace domain, the open loop transfer function can be calculated as below:

$$H_{Droop+LPF}(s) = \frac{\omega}{T_m} = \frac{k_p}{1 + T_f \cdot s} \tag{5.22}$$

Rewriting the above equation,

$$H_{Droop+LPF}(s) = \frac{\omega}{T_m} = \frac{1}{\frac{1}{k_p} + \frac{T_f}{k_p} \cdot s} \tag{5.23}$$

By comparing Equations 5.23 and 5.10, it can be concluded that the SME-EDC is quantitatively equivalent to the Droop with a low-pass filter [7]. The bode plot for Equations 5.9, 5.10 and 5.22 is illustrated in Fig. 5.7.

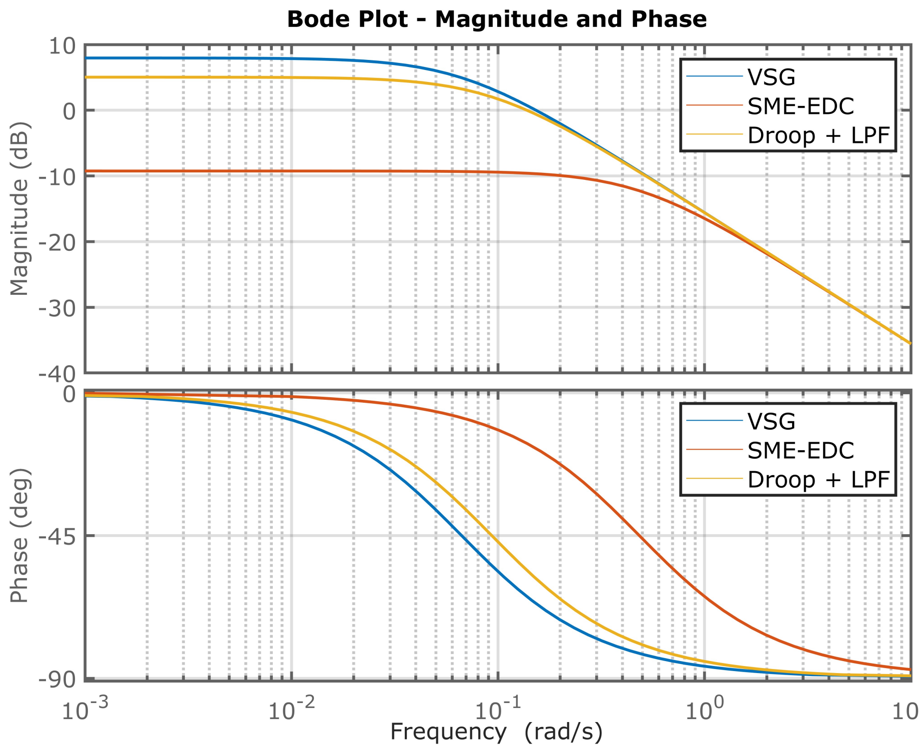

Figure 5.7: Bode plot for (a) VSG, (b) SME-EDC, (c) Droop with low pass filter with same inertia and damping

From Fig. 5.7, it can be concluded that the droop with a low-pass filter provides an equivalent response compared to the traditional VSG or SME-EDC controller.

However, due to the steady state error as mentioned in Equation 5.21, the effective damping decreases. This makes droop with a low pass filter quantitatively equal to VSG but not to be exact. To improve this, a steady state error term is introduced as mentioned in Fig. 5.8. This error term increases the effective damping and improves the stability of the system. The Bode plot with improved error term is illustrated in Fig. 5.9.

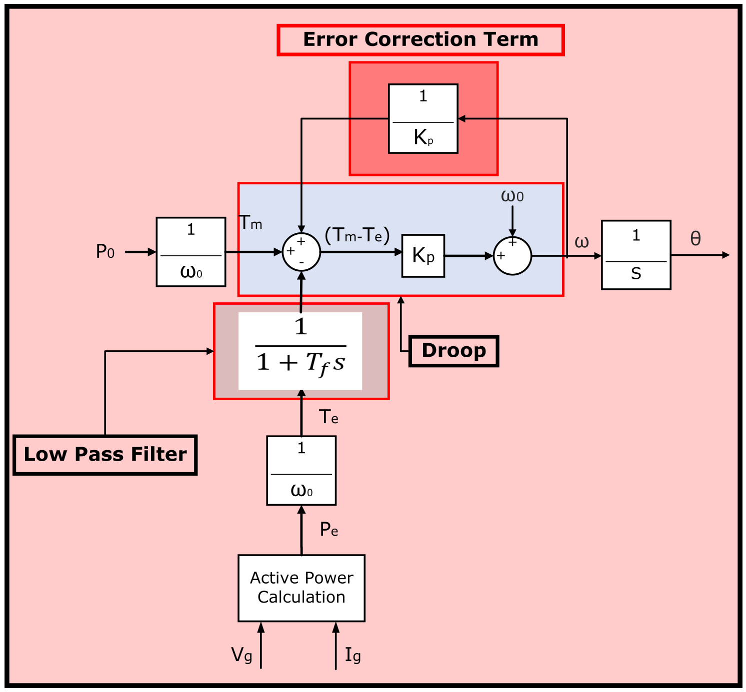

Figure 5.8: Block diagram of EnDC-InSME

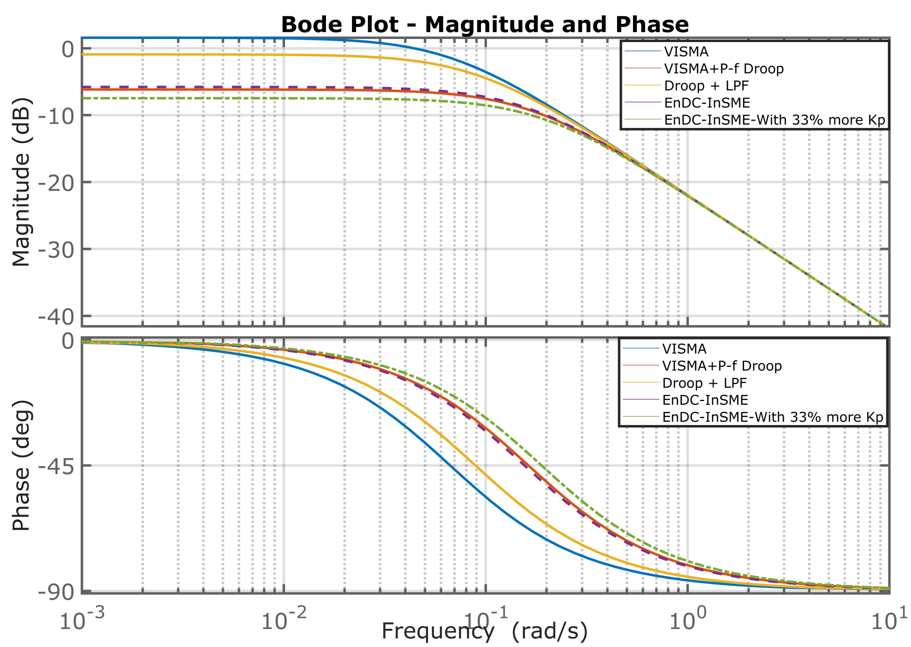

Figure 5.9: Bode plot for (a) VSG, (b) SME-EDC, (c) Droop + LPF, and (d) EnDC-InSME (e) EnDC-InSME with 33% more k_p

From 5.9, it is observed that the increment in k_p also changes the sensitivity of the system and the overall response of the controller. Hence, proper tuning of k_p and T_f is required, to obtain required virtual damping and inertia.

5.5 Small Signal Stability of EnDC-InSME using Eigenvalue Analysis and Step Response

Let's assume the state space variables as x_1 and x_2. To represent the Equation 5.18 into δ, the angular speed is the change in the rotor angle with respect to time so,

$$\omega = \frac{d\delta}{dt} \tag{5.24}$$

$$T_m - T_e = \frac{1}{k_p} \cdot \frac{d\delta}{dt} + \frac{T_f}{k_p}\frac{d\delta^2}{dt^2} - \frac{\omega_0}{k_p} \tag{5.25}$$

So let's say,

$$x_1 = \delta; \quad x_2 = \dot{x_1} = \dot{\delta} \tag{5.26}$$

$$T_m - T_e = \frac{1}{k_p} \cdot x_2 + \frac{T_f}{k_p}\dot{x_2} - \frac{\omega_0}{k_p} \tag{5.27}$$

$$T_m - T_e - \frac{1}{k_p} \cdot x_2 + \frac{\omega_0}{k_p} = \frac{T_f}{k_p}\dot{x_2} \tag{5.28}$$

$$\dot{x_2} = \frac{k_p}{T_f} \cdot \left[T_m - T_e - \frac{1}{k_p} \cdot x_2 + \frac{\omega_0}{k_p} \right] \tag{5.29}$$

Now by writing into state space form:

$$\frac{d}{dt}\begin{bmatrix} x_1 \\ x_2 \end{bmatrix} = \begin{bmatrix} 0 & 1 \\ 0 & \frac{-1}{T_f} \end{bmatrix} \cdot \begin{bmatrix} x_1 \\ x_2 \end{bmatrix} + \begin{bmatrix} 0 \\ \frac{T_m - T_e}{\frac{T_f}{k_p}} + \frac{\omega_0}{T_f} \end{bmatrix} \tag{5.30}$$

The Equation 5.30 can be rewritten as:

$$\frac{d}{dt}\begin{bmatrix} x_1 \\ x_2 \end{bmatrix} = \begin{bmatrix} 0 & 1 \\ 0 & \frac{-1}{T_f} \cdot \frac{k_p}{k_p} \end{bmatrix} \cdot \begin{bmatrix} x_1 \\ x_2 \end{bmatrix} + \begin{bmatrix} 0 \\ \frac{T_m - T_e}{\frac{T_f}{k_p}} + \frac{\omega_0}{T_f} \end{bmatrix} \tag{5.31}$$

$$\frac{d}{dt}\begin{bmatrix} x_1 \\ x_2 \end{bmatrix} = \begin{bmatrix} 0 & 1 \\ 0 & \frac{-1}{k_p} \cdot \frac{1}{\frac{T_f}{k_p}} \end{bmatrix} \cdot \begin{bmatrix} x_1 \\ x_2 \end{bmatrix} + \begin{bmatrix} 0 \\ \frac{T_m - T_e}{\frac{T_f}{k_p}} + \frac{\omega_0}{T_f} \end{bmatrix} \tag{5.32}$$

$$\frac{d}{dt}\begin{bmatrix} x_1 \\ x_2 \end{bmatrix} = \begin{bmatrix} 0 & 1 \\ 0 & \frac{-1}{T_f} \cdot \frac{k_p}{k_p} \end{bmatrix} \cdot \begin{bmatrix} x_1 \\ x_2 \end{bmatrix} + \begin{bmatrix} 0 \\ \frac{T_m - T_e}{\frac{T_f}{k_p}} + \frac{\omega_0}{T_f} \end{bmatrix} \tag{5.33}$$

$$\textbf{Droop with LPF:}\quad \frac{d}{dt}\begin{bmatrix} x_1 \\ x_2 \end{bmatrix} = \begin{bmatrix} 0 & 1 \\ 0 & \frac{-B_{EnDC-InSME}}{J_{EnDC-InSME}} \end{bmatrix} \cdot \begin{bmatrix} x_1 \\ x_2 \end{bmatrix} + \begin{bmatrix} 0 \\ \frac{T_m - T_e}{\frac{T_f}{k_p}} + \frac{\omega_0}{T_f} \end{bmatrix} \tag{5.34}$$

Equation 5.34 is the state space equation of droop with low pass filter. In EnDC-InSME control, a error term is included as mentioned in Fig. 5.8, and during the steady state, the ω will be ω_0, so by incorporating this in Equation 5.34, we get the state space equation of EnDC-InSME.

$$\textbf{EnDC-InSME:}\quad \frac{d}{dt}\begin{bmatrix} x_1 \\ x_2 \end{bmatrix} = \begin{bmatrix} 0 & 1 \\ 0 & \frac{-B_{EnDC-InSME}}{J_{EnDC-InSME}} \end{bmatrix} \cdot \begin{bmatrix} x_1 \\ x_2 \end{bmatrix} + \begin{bmatrix} 0 \\ \frac{T_m - T_e}{\frac{T_f}{k_p}} \end{bmatrix} \tag{5.35}$$

By comparing the Equation 5.35 with standerd form $\dot{X} = AX + BU$,

$$A = \begin{bmatrix} 0 & 1 \\ 0 & \frac{-B_{EnDC-InSME}}{J_{EnDC-InSME}} \end{bmatrix} \tag{5.36}$$

To determine the eigenvalues, it is necessary to solve the characteristic equation.

$$det(A - \lambda \cdot I_{2X2}) = 0 \tag{5.37}$$

where the λ is a set of eigen value.

From the above equations,

$$det\left(\begin{bmatrix} 0 & 1 \\ 0 & \frac{-B_{EnDC-InSME}}{J_{EnDC-InSME}} \end{bmatrix} - \lambda \cdot \begin{bmatrix} 1 & 0 \\ 0 & 1 \end{bmatrix}\right) = 0 \tag{5.38}$$

$$det\left(\begin{bmatrix} -\lambda & 1 \\ 0 & \frac{-B_{EnDC-InSME}}{J_{EnDC-InSME}} - \lambda \end{bmatrix} - \right) = 0 \tag{5.39}$$

$$\lambda \cdot \left(\frac{B_{EnDC-InSME}}{J_{EnDC-InSME}} + \lambda\right) = 0 \tag{5.40}$$

So,

$$\lambda_1 = 0 \tag{5.41}$$

and,

$$\lambda_2 = \frac{-B_{EnDC-InSME}}{J_{EnDC-InSME}} \tag{5.42}$$

λ_1 is zero so the system will exhibit steady-state oscillations. And since λ_2 is negative real part only, it can be interpreted that the system is asymptotically stable. These observations can be also verified using the step response of the system.

The open loop step response and frequency deviation of Equations 5.34 and 5.35 are as shown in Fig. 5.10.

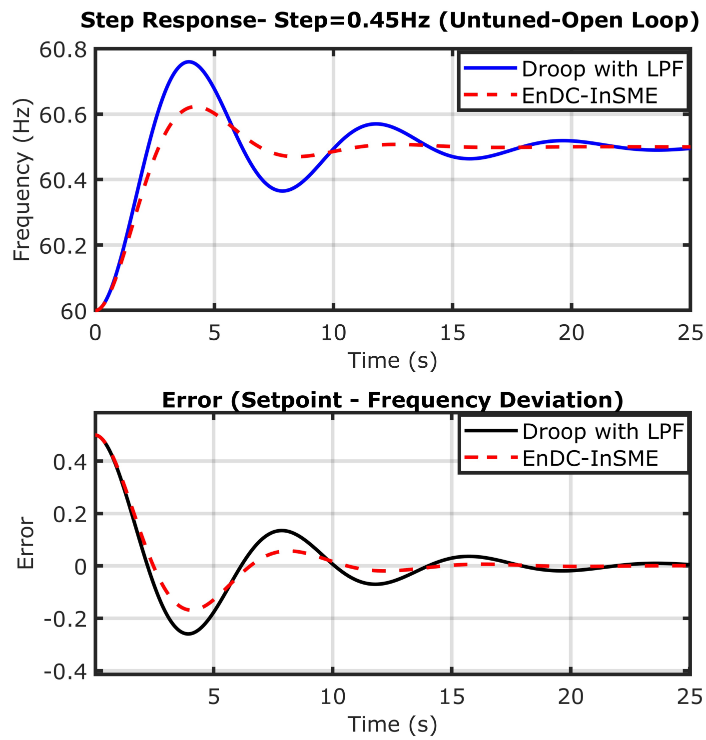

Figure 5.10: Frequency output of droop with LPF and EnDC-InSME with step input (Untuned)

In summary, all of the observations suggest that the EnDC-InSME exhibits more robust attainment of steady-state compared with a droop control with a low-pass filter. This characteristic proves that the EnDC-InSME is substantially more closely equivalently to VSG. The simulation and Hardware-in-loop results are briefly discussed in Chapter 6

In this section, the EnDC-InSME is simulated with a 3-phase, load-connected inverter. Section 6.1 outlines the inner control loops and its interaction with the outer EnDC-InSME and $Q - v$ droop loop. Section 6.2 shows the results obtained from MATLAB-SIMULINK under various conditions and briefly discusses the obtained results.

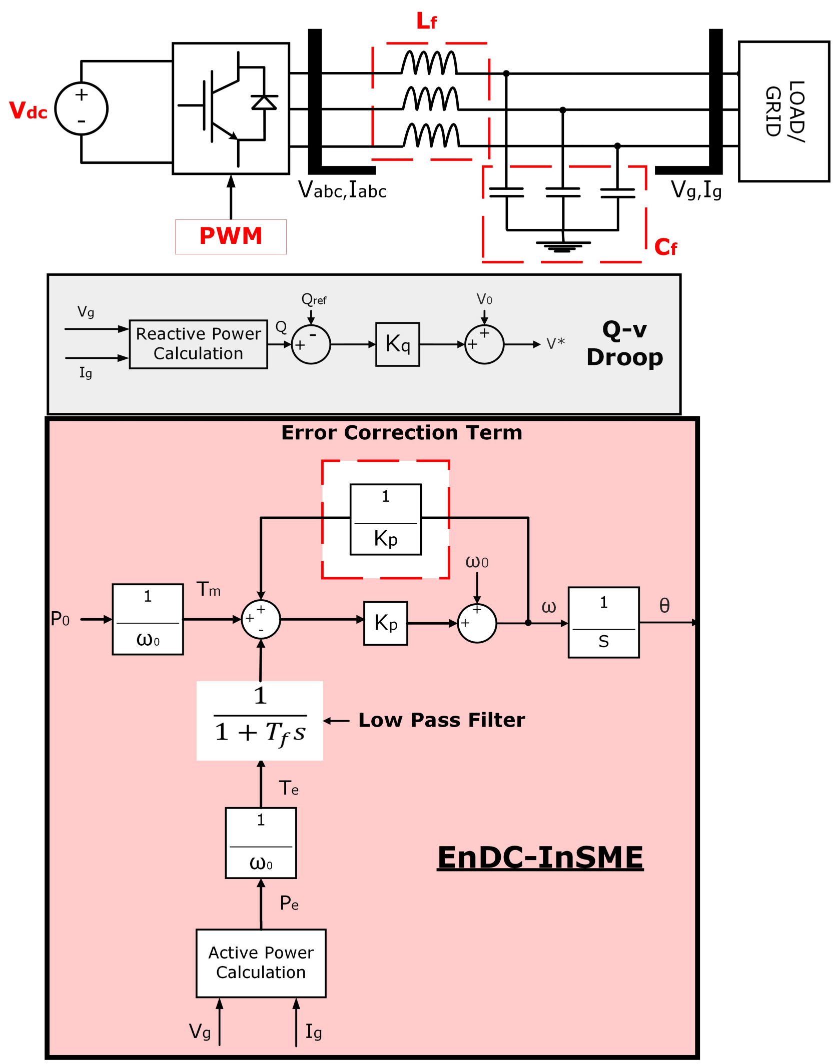

Figure 6.1: Block diagram of EnDC-InSME

6.1 Voltage & Current Control Loops

The θ and V^* are generated from EnDC-InSME and $Q-v$ droop as illustrated in Fig. 6.1 accordingly. An inner control loop is designed to regulate the voltage and current. A cascaded double loop is followed here to control the voltage at the PCC and current injection from the inverter to the load/grid. The outer loop consists of $Q-v$ droop and EnDC-InSME and the inner loop consists of a PI-regulated current control and voltage control as mentioned in Fig. 6.2.

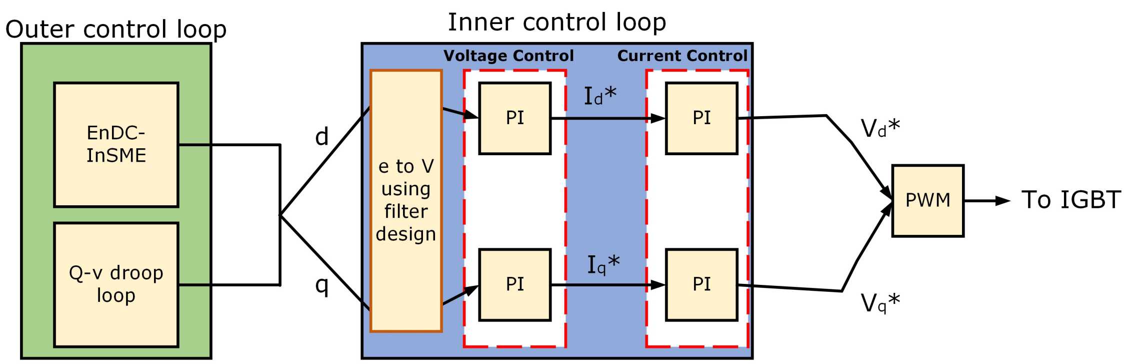

Figure 6.2: Block diagram of inner and outer control loops

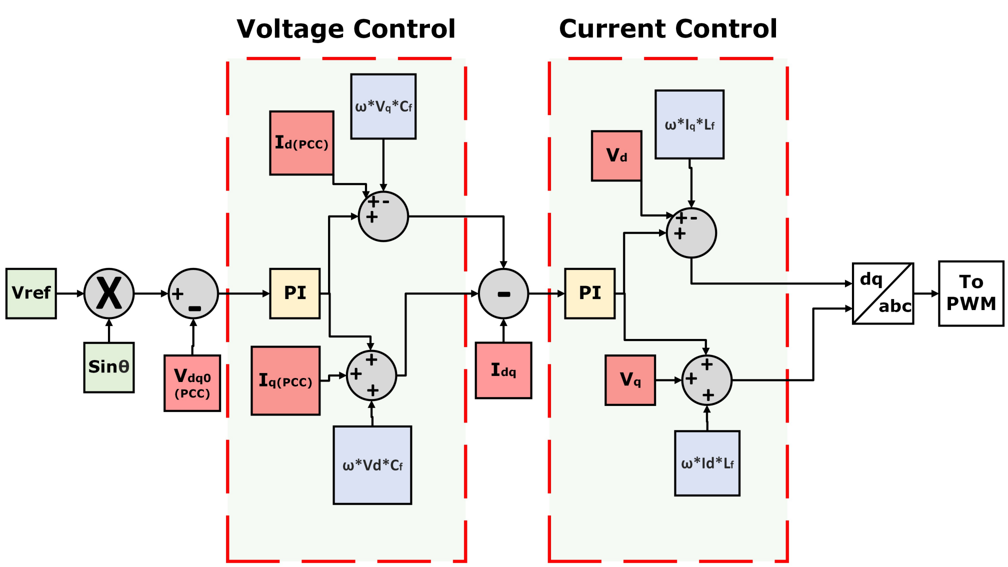

Figure 6.3: Detailed block diagram of voltage and current control in $d-q$ reference frame.

The voltage reference is taken from $Q-v$ droop along with θ reference from the

EnDC-InSME loop. These values are then fed to the double loop control which has embedded voltage control and current control. The detailed block diagram is illustrated in Fig. 6.3. The effect of virtual damping is also added by taking the filter parameters into account. This double loop control is robust and has greater control bandwidth compared with traditional current and voltage controls [20, 21].

6.2 MATLAB Simulation and Results

As illustrated in Fig. 6.4, a 3-phase voltage source connected with an LC filter and load is simulated in MATLAB/SIMULINK in a discrete domain. The L_f and C_f are calculated from the design equations mentioned in literature [22]. Table 6.1 mentions the circuit parameters and other tuning parameters.

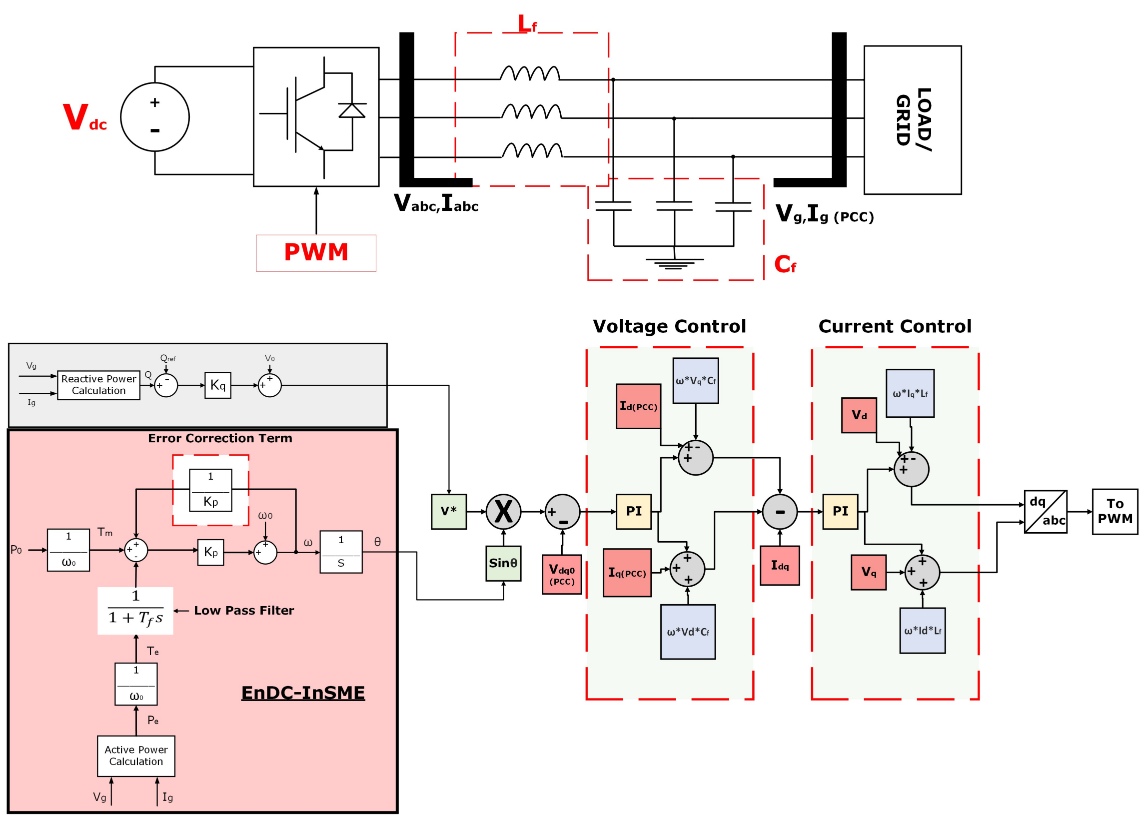

Figure 6.4: Block diagram for MATLAB simulation.

Table 6.1: Simulation Parameters

Name	**Value**	**Unit**
DC Voltage	800	V
L_f	18.45	mH
$R_{ESR(L)}$	100	Ω
C_f	100	μ F
$R_{ESR(C)}$	10	Ω
P_{Load1}	5000	W
P_{Load2}	6000	W
T_f (Time constant for LPF)	30	seconds
k_p (Droop Constant)$(P-f)$ [11, 2]	20	NA
k_v (Droop Constant) $(Q-v)$ [11, 2]	1000	NA
k_{p1} (k_p for first PI)	6.9587	NA
k_{i1} (k_i for first PI)	1.0124	NA
k_{p2} (k_p for second PI)	5.2364	NA
k_{i2} (k_i for second PI)	1.0547	NA
Switching frequency	10000	Hz
Simulation time-step	0.000001	seconds
Solver type	Fixed-step	NA

6.2.1 Test Condition-1: With Constant Load and Voltage Source

A constant voltage source is connected to a 3-phase inverter, which includes an L-C filter and a constant load of 8000 kW. The resulting AC voltage, current, frequency, and active power are mentioned in Fig. 6.5.

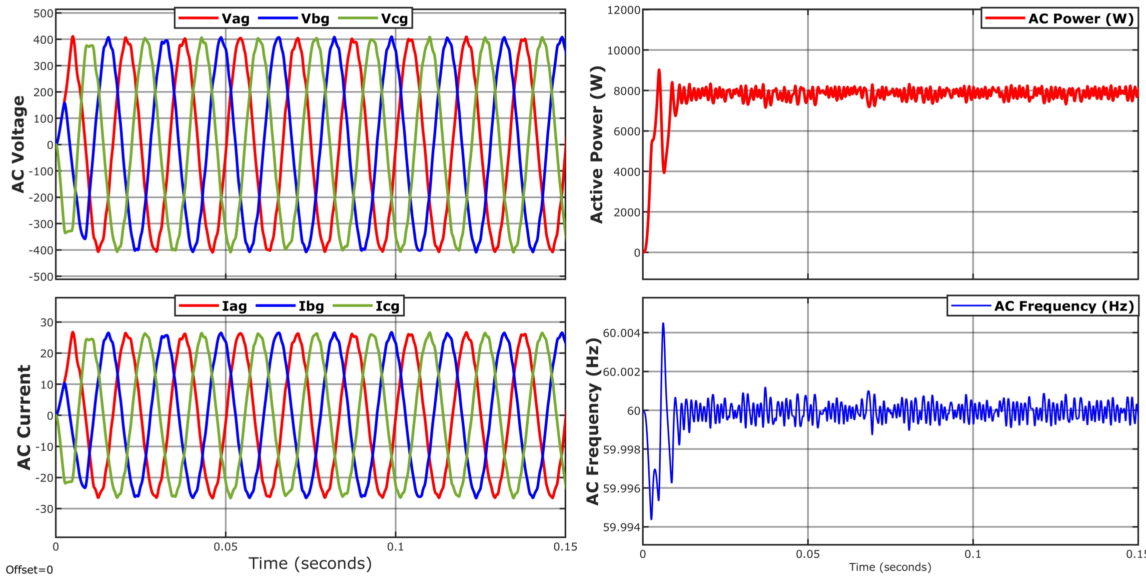

Figure 6.5: Inverter output with constant load

As illustrated in Fig. 6.5, the 3-phase AC voltage is synchronized, producing a clean sine wave. After 0.012 seconds, the system reaches a frequency of 60 Hz, with some steady-state oscillations. Concurrently, the active power stabilizes at 8 kW. Additionally, Fig. 6.6 demonstrates that the AC voltage of the grid-forming inverter is perfectly synchronized with that of the synchronous generator.

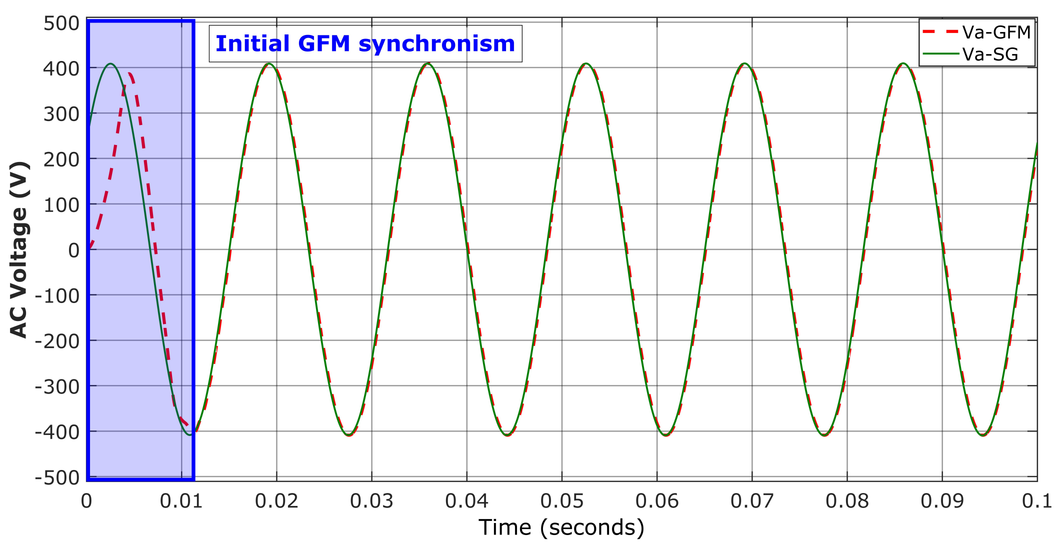

Figure 6.6: Output voltage of the SG and IBR under identical conditions.

6.2.2 Test Condition-2: With a Sudden Load Change

A constant voltage source is connected to a 3-phase inverter, including an L-C filter and an active load rapidly increasing by 20% at 0.25 seconds. The resulting AC voltage, current, frequency, and active power are depicted in Fig. 6.7.

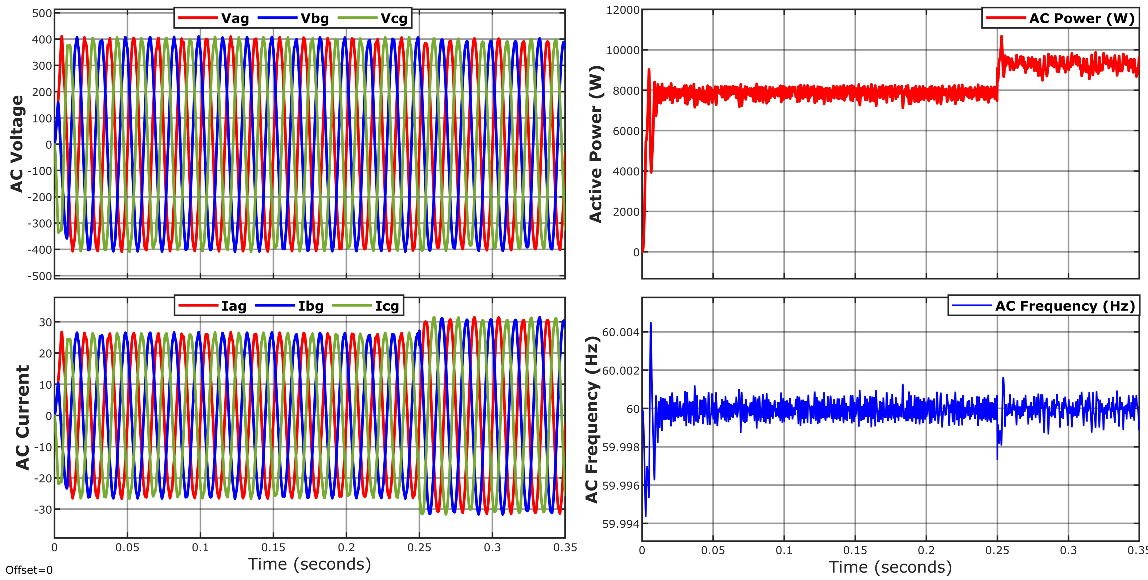

Figure 6.7: Inverter output with a 20% increment of load at 0.25 second.

As shown in Fig. 6.7, the AC voltage remains synchronized even after the sudden load change, producing a clean sine wave. Even after the rapid load change, the system reaches a frequency of 60 Hz, accompanied by some steady-state oscillations. Concurrently, the active power adjusts to accommodate the increased load. Fig. 6.8 shows a zoomed version when the load changes. It can be observed that the output frequency experiences a transient increase at 0.25 seconds due to the load change, but the frequency droop loop drives the system back to 60 Hz.

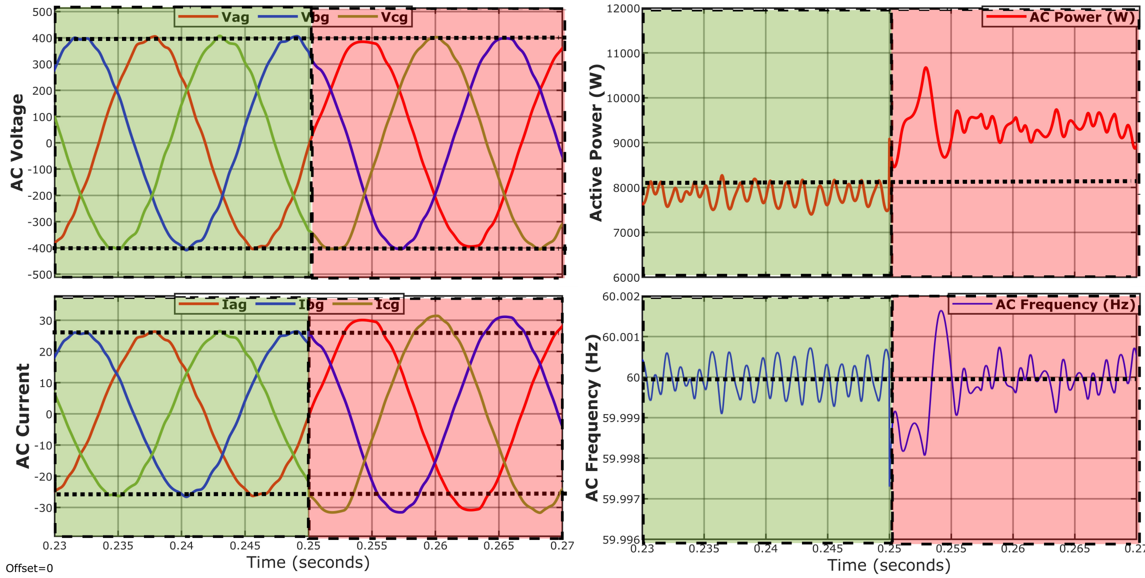

Figure 6.8: Zoomed inverter output with a 20% increment of load at 0.25 second.

Summarizing, the simulation results resonate effectively with the mathematical findings proposed in chapter 5, but further hardware testing is necessary to confirm the effectiveness of the control methodology.

CHAPTER 7: CONTROLLER HARDWARE-IN-LOOP

In this section, the proposed control methodology EnDC-InSME is tested in hardware in-loop (HIL) to verify the effectiveness of the control. In a Controller Hardware-In-Loop (CHIL), the control loops are being tested in a microcontroller and it is also linked to a power circuit being simulated in the real-time software. For this research, Texas Instruments' TI-Delfino 28335 is selected for the controller application, while the Typhoon HIL-604 serves as the real-time simulator. So, the TI-Delfino 28335 takes the voltage and current measurements to generate the PWM pulses for the inverter which is being simulated in real-time Typhoon HIL-604. Section 7.1 briefly discusses the CHIL approach, control configuration, and the results.

7.1 C-HIL Framework and Results

Fig. 7.1, represents the grid-cycle CHIL simulation cycle. As illustrated, the voltage and current measurements are first taken from Typhoon HIL 604. These measurements are scaled down to +/-3V and then converted to digital format according to the configurations of the Delfino controller. These measurements are then fed to the digital input pins of the Delfino 28335. The TI Delfino 28335 is real-time connected with MATLAB/SIMULINK's interface, from where all the control loops, DAC scaling, and ADC scaling are being deployed into TI Delfino 28335. These signals are converted to original form by converting into analog, and again scaling up in the 28335 controller. After these measurements are scaled up, the control loops are triggered, and as shown in chapter 6, the PWM pulses are generated. These pulses are then deployed to the real-time HIL 604, where the inverter's power circuit is running.

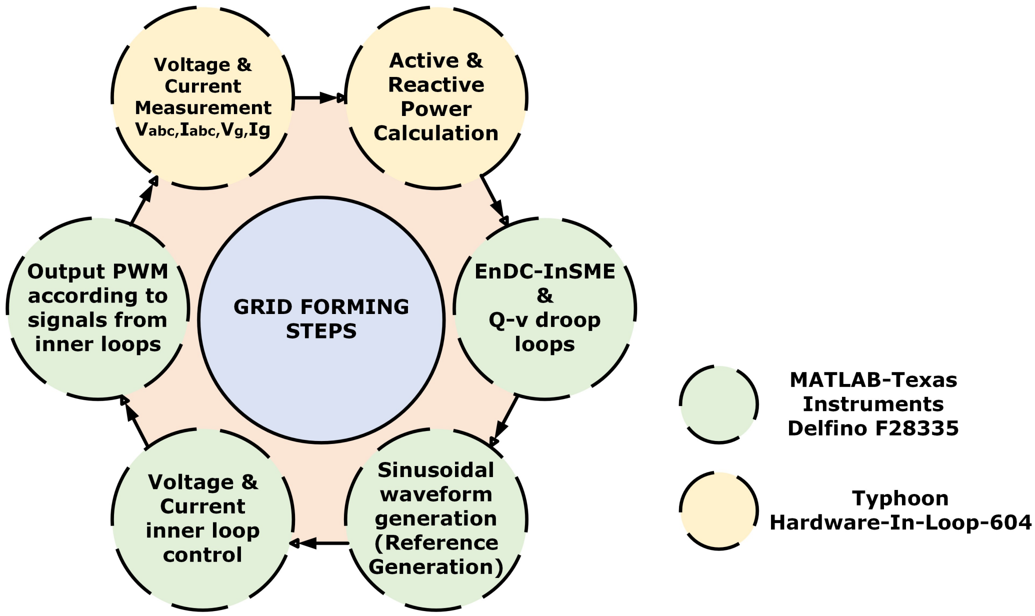

Figure 7.1: Controller-Hardware-In-Loop steps

The actual hardware setup is shown in 7.2, where the SIMULINK interface is being shown in the computer, which is connected with TI Delfino-28335 and Typhoon HIL 604. Detailed parameters of control elements and scaling are mentioned in table 7.1. The results of CHIL tests are shown in 7.4 and 7.3.

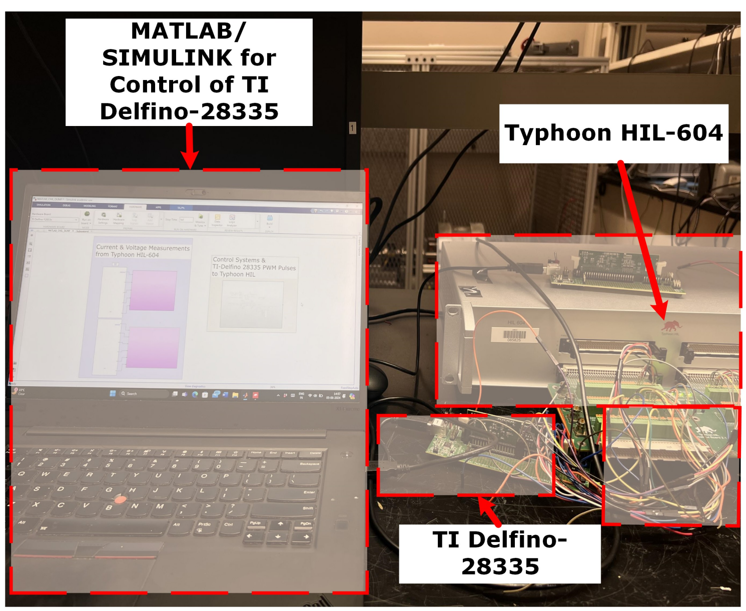

Figure 7.2: Test-bed for the CHIL experiment

Table 7.1: Controller Hardware-In-Loop parameters

Name	**Value**	**Unit**	**Origin of the data (Location)**
DC Voltage	800	V	Typhoon HIL-604
L_f	26.42	mH	Typhoon HIL-604
$R_{ESR(L)}$	100	Ω	Typhoon HIL-604
C_f	167	μF	Typhoon HIL-604
$R_{ESR(C)}$	10	Ω	Typhoon HIL-604
P_{LOAD1}	8000	W	Typhoon HIL-604
P_{LOAD2}	14000	W	Typhoon HIL-604
T_f	67	seconds	TI-Delfino 28335
k_p	14	NA	TI-Delfino 28335
k_v	1000	NA	TI-Delfino 28335
k_{p1}	7.4812	NA	TI-Delfino 28335
k_{i1}	1.57814	NA	TI-Delfino 28335
k_{p2}	5.6971	NA	TI-Delfino 28335
k_{i2}	1.24475	NA	TI-Delfino 28335
Switching Frequency for PWM	5000	Hz	TI-Delfino 28335
Controller time-step	50e-6	seconds	TI-Delfino 28335
HIL time-step	50e-6	seconds	Typhoon HIL-604
Solver Type	Fixed Step-Real Time	NA	TI-Delfino 28335
Scaling Factor for voltage	1/300	NA	Typhoon HIL-604
Scaling Factor for current	100/3	NA	Typhoon HIL-604
DC Offset for voltage and current	+3.67	V	Typhoon HIL-604

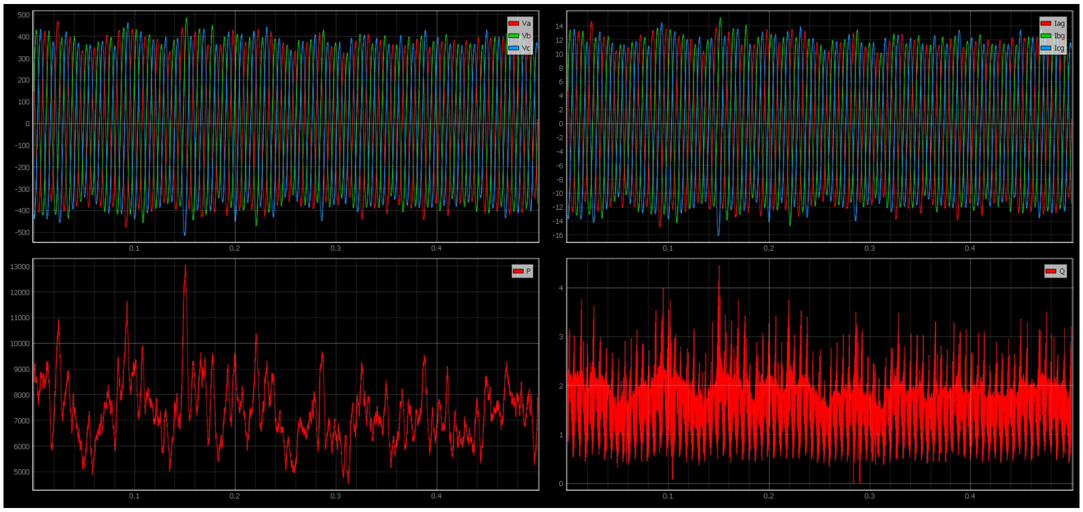

Figure 7.3: Controller Hardware-In-Loop results with load change

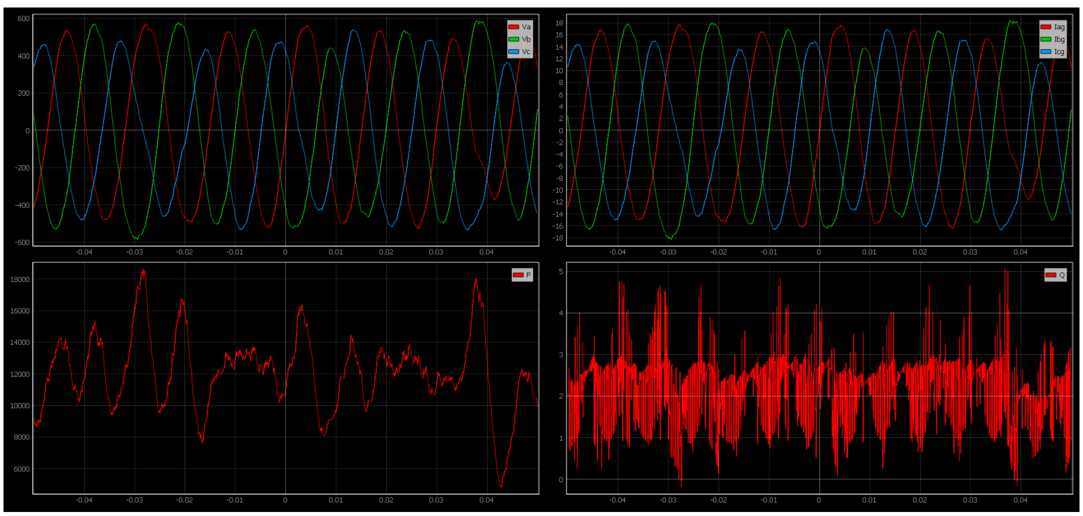

Figure 7.4: Controller Hardware-In-Loop results (Zoomed)

From Fig. 7.4 and 7.3 are the results under two different conditions. In Fig. 7.4, the load is 12000 W constant, while in 7.3, the load is constantly changing from 8000 W to 9500 W to check the response under rapidly changing loads.

As shown in Fig. 7.4, the 3-phase AC voltage remains almost synchronized, producing a clean sine wave. Concurrently, the current also stays synchronized, but due to the load change and the absence of closed-loop voltage control, the active power exhibits steady-state oscillations greater than expected from MATLAB simulations.

This issue can be mitigated with slower control loops. The reactive power shows some noise, contributing to voltage deviations. Fig. 7.3 demonstrates the behavior of the GFM under rapid load changes, revealing that the output voltage and current remain stable according to the load.

CHAPTER 8: CONCLUSIONS & FUTURE WORK

8.1 Conclusions

The concluding remarks of this thesis are as follows:

1. Grid-following V/s Grid-forming: A duality theory

   (a) Opposing Synchronizing loops: The $P-\omega$ droop control for a grid-forming inverter is equivalent to the $V_q-\omega$ loop embedded into PLL, which is further equivalent to $Q-\omega$ loop. These converse synchronizing loops make these inverters duals of each other.

   (b) Different grid interfacing characteristics. The grid interfacing behavior of the grid following inverter is grid voltage following, current forming (current source inverters), and for the grid forming inverters, grid voltage forming, current following (voltage source inverters).

2. Mathematical Justifications for Using a Low Pass Filter in Droop Control: Beyond Harmonic Filtering:

   (a) A low pass filter combined with droop control is essential for emulating grid-forming behavior. Mathematical justifications indicate that this configuration can quantitatively emulate a synchronous generator, but not exactly.

3. Enhanced Droop Control with Integrated Synchronous Machine Emulation for Grid-Forming Inverters:

   (a) Introducing an error correction term in droop control with a low pass filter makes the overall response equivalent to that of a synchronous generator.

   (b) By doing so, the enhanced droop integrates the synchronous generator, hence it improves stability and performance, especially during transient conditions.

   (c) Robust control loop: The stability and performance guarantee of the enhanced droop control were validated through the Bode plot, eigenvalue analysis, and step response.

4. Simulations and hardware validations:

   (a) The EnDC-InSME control methodology was simulated in SIMULINK using a 3-phase inverter connected to an L-C filter. Different operating and loading conditions were tested to evaluate the system's performance.

   (b) A real-time controller hardware-in-loop experiment was conducted to verify the results, ensuring the accuracy and reliability of the simulated performance under practical conditions.

8.2 Future Work

While the current research has significantly improved the traditional droop control strategies and their implementation, several areas need further investigation to improve the robustness and performance of the proposed system. The future work includes:

1. The low pass filter that is analyzed in this research is only connected with the active power-frequency droop, not with the reactive power-voltage droop. Further research is required to investigate the effect on $Q - v$ droop.

2. In this research, the inner voltage control loop does not guarantee voltage control during the no-load condition, so a closed loop voltage control is required to improve the applicability of the inverter.

These efforts will contribute to the development of more efficient and resilient grid-forming inverters, ultimately supporting the transition to a more sustainable and reliable power grid.

REFERENCES

[1] "Grid forming inverters: Epri tutorial. epri, palo alto, ca: 2021. 3002021722.."

[2] J. Liu, Y. Miura, and T. Ise, "Comparison of dynamic characteristics between virtual synchronous generator and droop control in inverter-based distributed generators," *IEEE Transactions on Power Electronics*, vol. 31, pp. 3600–3611, 05 2016.

[3] D. B. Rathnayake, M. Akrami, C. Phurailatpam, S. P. Me, S. Hadavi, G. Jayasinghe, S. Zabihi, and B. Bahrani, "Grid forming inverter modeling, control, and applications," *IEEE Access*, vol. 9, pp. 114781–114807, 2021.

[4] W. Du, Z. Chen, K. P. Schneider, R. H. Lasseter, S. Pushpak Nandanoori, F. K. Tuffner, and S. Kundu, "A comparative study of two widely used grid-forming droop controls on microgrid small-signal stability," *IEEE Journal of Emerging and Selected Topics in Power Electronics*, vol. 8, no. 2, pp. 963–975, 2020.

[5] P. Jahangiri and D. C. Aliprantis, "Distributed volt/var control by pv inverters," *IEEE Transactions on Power Systems*, vol. 28, no. 3, pp. 3429–3439, 2013.

[6] Y. Li, Y. Gu, and T. C. Green, "Revisiting grid-forming and grid-following inverters: A duality theory," *IEEE Transactions on Power Systems*, vol. 37, no. 6, pp. 4541–4554, 2022.

[7] B. Bahrani, M. H. Ravanji, B. Kroposki, D. Ramasubramanian, X. Guillaud, T. Prevost, and N.-A. Cutululis, "Grid-forming inverter-based resource research landscape: Understanding the key assets for renewable-rich power systems," *IEEE Power and Energy Magazine*, vol. 22, no. 2, pp. 18–29, 2024.

[8] W. Yao, M. Chen, J. Alcala, J. Guerrero, and Z.-M. Qian, "Design and analysis of the droop control method for parallel inverters considering the impact of the complex impedance on the power sharing," *Industrial Electronics, IEEE Transactions on*, vol. 58, pp. 576 – 588, 03 2011.

[9] J. Guerrero, L. de Vicuna, J. Matas, M. Castilla, and J. Miret, "A wireless controller to enhance dynamic performance of parallel inverters in distributed generation systems," *IEEE Transactions on Power Electronics*, vol. 19, no. 5, pp. 1205–1213, 2004.

[10] J. Liu, Y. Miura, and T. Ise, "Comparison of dynamic characteristics between virtual synchronous generator and droop control in inverter-based distributed generators," *IEEE Transactions on Power Electronics*, vol. 31, no. 5, pp. 3600–3611, 2016.

[11] P. R. Chowdhury, E. Shoubaki, and M. Manjrekar, "Modified voltage and frequency control of parallel-connected grid-forming inverters by virtual synchronous machine controller," in *2020 IEEE International Conference on Power Electronics, Drives and Energy Systems (PEDES)*, pp. 1–5, 2020.

[12] S. V. Dhople, B. B. Johnson, and A. O. Hamadeh, "Virtual oscillator control for voltage source inverters," in *2013 51st Annual Allerton Conference on Communication, Control, and Computing (Allerton)*, pp. 1359–1363, 2013.

[13] Y. Han, H. Ye, Z. Guo, J. Zhao, W. Pei, and J. Xiong, "Control strategy of virtual oscillators with adjustable tie line power in interconnected system," *Energy Reports*, vol. 9, pp. 359–367, 2023. 2022 2nd International Joint Conference on Energy and Environmental Engineering.

[14] M. Ahmed, F. Alsokhiry, A. S. Abdel-Khalik, K. H. Ahmed, and Y. Al-Turki, "Improved damping control method for grid-forming converters using lqr and optimally weighted feedback control loops," *IEEE Access*, vol. 9, pp. 87484–87500, 2021.

[15] Y. Li, Y. Gu, Y. Zhu, A. Junyent-Ferre, X. Xiang, and T. C. Green, "Impedance circuit model of grid-forming inverter: Visualizing control algorithms as circuit elements," *IEEE Transactions on Power Electronics*, vol. 36, no. 3, pp. 3377–3395, 2021.

[16] S. D'Arco and J. A. Suul, "Equivalence of virtual synchronous machines and frequency-droops for converter-based microgrids," *IEEE Transactions on Smart Grid*, vol. 5, no. 1, pp. 394–395, 2014.

[17] C. Arghir and F. Dorfler, "The electronic realization of synchronous machines: Model matching, angle tracking, and energy shaping techniques," *IEEE Transactions on Power Electronics*, vol. 35, no. 4, pp. 4398–4410, 2020.

[18] T. Liu and X. Wang, "Physical insight into hybrid-synchronization-controlled grid-forming inverters under large disturbances," *IEEE Transactions on Power Electronics*, vol. 37, no. 10, pp. 11475–11480, 2022.

[19] R. H. Lasseter, Z. Chen, and D. Pattabiraman, "Grid-forming inverters: A critical asset for the power grid," *IEEE Journal of Emerging and Selected Topics in Power Electronics*, vol. 8, no. 2, pp. 925–935, 2020.

[20] C. Kalavalli, P. Meenalochini, S. Pallakku, and S. Haq, "Dual loop control for single phase pwm inverter for distributed generation," *Materials Today: Proceedings*, vol. 45, 11 2020.

[21] Q. Peng, H. Pan, Y. Liu, and L. Xiang, "Dual-loop control strategy for grid-connected inverter with lcl filter," *Energy and Power Engineering*, vol. 05, pp. 97–101, 01 2013.

[22] X. Li, Z. Deng, Z. Chen, and Q. Fei, "Analysis and simplification of three-dimensional space vector pwm for three-phase four-leg inverters," *IEEE Transactions on Industrial Electronics*, vol. 58, no. 2, pp. 450–464, 2011.